2019

Broadband Mid-infrared Frequency Combs Generated via Frequency Division

Qitian Ru
University of Central Florida

BROADBAND MID-INFRARED FREQUENCY COMBS GENERATED VIA FREQUENCY DIVISION

by

QITIAN RU

B.S. Zhejiang University, 2011

M.S. East China Normal University, 2014

M.S. University of Central Florida, 2018

A dissertation submitted in partial fulfilment of the requirements
for the degree of Doctor of Philosophy
in CREOL, the College of Optics and Photonics
at the University of Central Florida
Orlando, Florida

Summer Term

2019

Major Professor: Konstantin L. Vodopyanov

ABSTRACT

Frequency combs have revolutionized metrology and demonstrated numerous applications in science and technology. Combs operating in the mid-infrared region could be beneficial for molecular spectroscopy for several reasons. First, numerous molecules have their spectroscopic signatures in this region. Furthermore, the atmospheric window (3-5μm and 8-14μm) is located here. Additionally, a mid-infrared frequency comb could be employed as a diagnostic tool for the many components of human breath, as well as for detection of harmful gases and contaminants in the atmosphere. In this thesis, I used synchronously pumped subharmonic optical parametric oscillators (OPOs) operating at degeneracy to produce ultra-broadband outputs near half of the pump laser frequency. One attractive property of the subharmonic OPOs is that the signal/idler waves of the OPO are frequency- and phase-locked to the pump frequency comb. We explored three new nonlinear materials in the subharmonic OPO and demonstrated a broadband spectrum for mid-infrared frequency comb generation. (1) Orientation-patterned (OP) gallium arsenide (GaAs) was selected as the first material because it has high nonlinearity. We found that the OP-GaAs based OPO yielded an approximately two-octave wide spectrum (2.8–11μm). (2) Gallium phosphide (GaP) has near zero group velocity dispersion (GVD) at 4.7 μm and a large bandgap. The OP-GaP OPO yielded a spectrum of more than two octaves (3–12.5μm). Also, because of the large bandgap, GaP is suitable for telecom 1.56-μm pumping, having the advantage of much smaller GVD than in periodically-poled-lithium-niobite (PPLN). The telecom laser (1.56μm) pumped OP-GaP OPO was demonstrated with more than one octave wide spectrum. (3) Finally, we explored the phenomenon of random phase matching in the zinc selenide (ZnSe)

polycrystalline material. The first random phase matched OPO was demonstrated with more than one octave spectrum (3.1– 9μm), which is also the first OPO based on ZnSe.

To my family

ACKNOWLEDGMENTS

First and foremost, I would like to offer my deepest thanks to my Ph.D. advisor Dr. Konstantin Vodopyanov for his support, kindness, patience, and excellent advice throughout these years of graduate study. It has been so satisfying to work and study under such a knowledgeable scientist.

Next, I wish to express my gratitude towards my committee members, Dr. Shin-Tson Wu, Dr. Sasan Fathpour, and Dr. Robert Peale for their consistent support and patience throughout the dissertation process. I would also like to extend my gratitude towards the late Dr. Boris Zeldovich for his contribution to my committee before his passing and for his class that I thoroughly enjoyed.

I also want to acknowledge the College of Optics and Photonics (CREOL) at the University of Central Florida (UCF). This department is truly world-class and has also made me feel like I have been part of a family. I particularly want to show appreciation for staff members, including Rachel, Amy, Gail, Alma and etc. for their exceeding levels of friendliness throughout my years at CREOL.

Throughout my time at CREOL, I have had the opportunity to work with some outstanding graduate students and scientists. Therefore, I would like to recognize Andrey Muraviev, Zachary Loparo, Taiki Kawamori, Nathan Lee, and Xuan Chen. I also wish to thank Sergey Vasilyev and Sergey Mirov from IPG Photonics for providing excellent lasers and ceramics as well as Peter Schunemann for his superb-quality crystals.

Finally, the completion of this dissertation would not have been possible without the support of my loving family. I am so incredibly grateful to my parents for providing their unconditional love

and encouragement during my Ph.D. studies. Also, I am eternally thankful for the constant support, love, and determined faith that my dear wife has shown me throughout the dissertation process.

Thank you again from the bottom of my heart to everyone listed here for helping me to transform this dissertation from a dream to a reality.

TABLE OF CONTENTS

LIST OF FIGURES

CHAPTER ONE: INTRODUCTION

1.1 Frequency Comb

Frequency combs provide unparalleled speed and precision. The Nobel Prize in Physics 2005 was half awarded to John L. Hall and Theodor W. Hänsch jointly "for their contributions to the development of laser-based precision spectroscopy, including the optical frequency comb technique". Frequency combs are essentially evenly spaced time pulses in the time domain. The Fourier transform of these pulses corresponds to evenly spaced lines in the frequency domain. The development of frequency combs was reviewed in great detail in the Nobel Prize lecture by Hänsch [1] and Hall [2].

Frequency combs have revolutionized metrology. Initially they were developed for frequency metrology, working as a gear for optical atomic clocks. Then, people started using them in a wide range of applications [3] including, nonlinear spectroscopies [4, 5], ultraviolet and infrared spectroscopy [6-9], optical and microwave generation, astronomical spectrograph calibration, attosecond pulse generation, and test of quantum electrodynamics by precision metrology of hydrogen molecules [10] etc., because frequency combs offers a combination of high brightness, broad bandwidth, high spectral resolution, and fast readout.

Dual-combs system have lots advantages, such as moving-part-free, compared to the traditional Fourier-transform infrared spectroscopy. Dual-combs system with a broadband output have been utilized to measure a mixer of gases with a great signal to noise ratio [11, 12]. Up to 22 trace molecular species have been parallelly detected with part-per-billion sensitivity and sub-Doppler resolution [11].

1.2 Mid-Infrared Region

Frequency combs operating in the mid-infrared (2 – 20 μm) region could be beneficial for molecular spectroscopy for several reasons[13, 14]. First, numerous molecules have their spectroscopic signatures in this region. Most molecules have intense fundamental vibrational band in the mid-infrared region. This strength of the transitions in the mid-infrared region may be more than a thousand-fold stronger than it in the near-infrared telecom region, which will enhance the detection sensitivity in a similar proportion. This region is also called "fingerprint region" because these unique spectral features can be used to identify those molecules, like the smart phone identifies the user using their fingerprints. Or one can think of them as the UPC barcodes located on the items sold in supermarkets.

Furthermore, the atmospheric window (3-5 μm and 8-14 μm) is located here. Additionally, a mid-infrared frequency comb could be employed as a diagnostic tool for the many components of human breath, as well as for detection of harmful gases and contaminants in the atmosphere.

The most common mid-infrared light source is black-body radiation. However, due to the lack of coherent sources and the presence of high thermal background radiation, obtaining optical measurements in this region is rather difficult.

1.3 Mid-Infrared Sources

Black-body radiation: black-body radiation is the thermal electromagnetic radiation within or surrounding a body that it is in thermodynamic equilibrium with its environment or emitted by a black body. The spectrum of the black-body radiation only depends on the body's temperature (Planck's law).

Quantum cascaded lasers (QCLs): QCLs are semiconductor mid-infrared lasers. They use the intersubband transitions to reduce the photon energy, as opposed to earlier mid-infrared semiconductor lasers that were based on interband transitions. The wavelength of the QCL lasers can be tuned by a wide range by engineering the details of the semiconductor layer structure.

Interband Cascade lasers (ICLs): ICLs are a type of laser diode that produce coherent radiation over a large part of the mid-infrared region of the electromagnetic spectrum. The photons are generated with the interband transitions, rather than the intersubband transitions used in QCLs. The threshold current density is lower in ICLs than in QCLs, because of the difference in carrier lifetimes.

Doped Insulator Lasers: there are only a few types of doped insulator solid-state lasers, such as 1) Cr^{2+}:ZnS/ZnSe lasers. They can emit 1.9-3.3 μm. They are broadly tuned and can easily produce hundreds of milliwatts of output power. 2) Fe^{2+}:ZnSe lasers. They can emit 3.7-5.1 μm. 3) Fiber lasers based on the erbium-doped or holmium-doped fluoride fibers. They emit at ~3μm.

Sources based on difference frequency generation (DFG): a wide tunable range of the mid-infrared region can be generated by DFG in a nonlinear crystal. This usually requires two laser beams with different frequencies.

Non-degenerated OPOs: OPOs are nonlinear frequency conversion devices which starts with a single near-infrared laser. The generated signal and idler waves can be in the mid-infrared spectral region. In nondegenerate OPOs, the signal wave and idler wave have different frequencies. The OPO is essentially a photon splitter, which splits a higher energy photon into two low energy

photons. Compared to different frequency generations, in OPOs, the conversion efficiency is dramatically improved due to the resonant cavity. However, in the nondegenerate OPO, active feedback loop is required to stabilize the CEO frequency of the idler wave [15]. A singly resonant OPO based on PPLN operating at 2.8 – 4.8 μm has been demonstrated with exciting molecular spectroscopy result recently [16-18].

Degenerate OPOs: in a degenerate OPO, the signal wave and idler wave are indistinguishable from each other. Thus, the frequency and the phase of the signal/idler wave are intrinsically locked to the pump comb. No extra feedback loop is required to stabilize the CEO frequency of the signal/idler wave. In addition, degenerate OPOs have an extremely low pump threshold compared to singly resonant OPOs, which helps greatly augment the spectrum bandwidth. In this thesis, we will use doubly resonant OPOs to shift frequency combs in the near-infrared region to the mid-infrared region.

CHAPTER TWO: SUBHARMONIC OPTICAL PARAMETRIC OSCILLATORS

2.1 Subharmonic OPOs

Most OPOs works in non-degenerate mode. When the signal and idler waves are pushed together and become indistinguishable, the OPO works in the degenerate mode. We call it subharmonic OPO. This OPO will be intrinsically phase locked to the pump laser and augment the spectrum bandwidth. Subharmonics oscillation was already observed in acoustic and mechanics since the 19th century. Faraday observed the frequency standing wave of a liquid surface is half of the applied force [19]. Reduced models developed to study the synchronously pumped subharmonic OPOs [20].

In an OPO, the photon energy conservation dictates that [21]:

$$\nu_p = \nu_s + \nu_i \qquad (1)$$

The phase relationship between the pump, signal and idler waves is:

$$\phi_p = \phi_s + \phi_i + \frac{\pi}{2} \qquad (2)$$

Here $\nu_p, \nu_s, and\ \nu_i$ are the pump, signal and idler frequencies. $E_p = E_p \cos(2\pi\nu_p t + \phi_p)$, $E_s = E_s \cos(2\pi\nu_s t + \phi_s)$, and $E_i = E_i \cos(2\pi\nu_i t + \phi_i)$ are the electric fields of the pump, signal and idler, correspondingly. For a non-degenerate OPO, the signal and the older phases, ϕ_s and ϕ_i, are free to adopt any value as long as equation (2) is satisfied. The π/2 in the equation is to ensure the energy flow from the pump wave to the signal and idler waves [22].

The degree of freedom disappears when the (co-polarized) signal and idler become indistinguishable, which leads to $\phi_s = \phi_i$. Then equation (2) becomes

$$\phi_p = 2\phi_{s,i} + \frac{\pi}{2} \quad (3)$$

The phase coherence between the OPO and the pump is established.

The pump field is represented by a frequency comb,

$$\nu_n = f_{CEO} + nf_{rep} \quad (4)$$

with mode separation f_{rep} corresponding to the pulse repetition rate, n as the mode number (typical n is 10^6 – 10^7). And f_{CEO} is the carrier-envelope offset (CEO). For degenerated OPO, the output frequency comb is

$$\nu_m = \frac{f_{CEO}}{2} + mf_{rep} \quad (5)$$

or

$$\nu_m = \frac{f_{CEO}}{2} + (m + \frac{1}{2})f_{rep} \quad (6)$$

Here m is the OPO mode number (centered around some m_0, which is the closet integer to $n_0/2$).

To obtain a broadband spectrum in the degenerate OPO, there are several parameters that should be considered. 1) the acceptance bandwidth of the nonlinear crystal. 2) the extra phase of the cavity. 3) the reflection of the mirror.

The acceptance bandwidth of the crystal is caused by the chromatic dispersion of the crystal. Phase matching can be achieved only in a limited bandwidth because of the group velocity mismatch of the interacting waves. For quasi phase matching (QPM) crystals, usually the real QPM period is slightly different from the ideal phase matching period to achieve a larger bandwidth.

The cavity mode spacing is determined by the derivative of the extra phase of the cavity. The mode-locked laser has the equidistance spaced Longitudinal modes on the frequency axis. Due to the dispersion elements in the OPO cavity, there is a mismatch between the cavity modes and laser modes. This will cause loss for those mismatched modes and reduce the bandwidth of the output wave.

The reflection bandwidth of the mirror is another important factor in limiting the bandwidth of the OPO. Usually, the pump beam is incoupled in to the OPO cavity through a dielectric mirror, which highly transmits the pump wave and highly reflects the signal and idler waves. However, increasing the reflection bandwidth will also increase the thickness of the optical coating on the dielectric mirror. This will greatly increase the cavity dispersion and decrease the bandwidth of the OPO. In our lab, we use a pump injector to incouple the pump laser into the cavity.

Subharmonic OPOs are suitable to generate broadband mid-infrared frequency combs . In 2011, subharmonic OPO based on periodically poled lithium niobate (PPLN) was demonstrated with spectrum spanning 2.5 - 3.8 μm [23]. OP-GaAs based subharmonics OPO pumped by 2 μm laser has been demonstrated with a spectrum spanning 2.6 – 6.1 μm in 2012 [24] and 2.6 – 7.5 μm in 2016 [25]. OP-GaAs OPO pumped by ~2.4 μm Cr:ZnS and Cr:ZnSe laser has yield spectrum ranging 4.4 – 5.4 μm in 2011 [26] and 3.3 – 5.6 μm in 2015 [27].

2.2 Coherent Properties of the Subharmonics OPOs

In the past, OPOs were used to extend the near infrared frequency combs to the mid infrared region [16, 28]. These singly resonant OPOs demonstrated great potential to generate the broad range mid-infrared combs. However, an extra phase lock loop was required to lock the singly resonant OPO and the spectra had a narrow bandwidth.

Subharmonic OPOs are an alternative way to generate a broad bandwidth spectrum, thanks to their low pump threshold, low dispersion and broadband parametric gain bandwidth. Their coherent properties were studies in great detail [29]. Subharmonics OPO have two states which have a difference of the frequency of half of repetition rate. The phase of the OPO is random. It was detailed studied [29, 30]. The relative linewidth between the output of subharmonic OPO and the pump comb was measured less than 1Hz which proved the preservation of the comb nature of the pump [31, 32].

2.3 Quasi-phase-matching

Quasi-phase-matching (QPM) was first theoretically introduced by Armstrong et al. [22]. However, QPM was only intensively used after 1980s thanks to the breakthrough of periodic poling. The development of QPM is reviewed by Hu et al. [33]. In 1995, Myers et al. demonstrated the first bulk QPM OPO using periodically pooled $LiNbO_3$ (PPLN) pumped by 1 μm laser [34]. In 1997, Galvanauskas et al. demonstrated the first femtosecond QPM OPO in PPLN with 300-fs pulse duration [35].

To use the crystals without birefringence, such as GaAs, in OPOs, QPM is required. QPM crystal is a method to achieve the non-critical phase match by spatially modulating the nonlinear

properties of the material. In QPM crystals, the sign of the nonlinear coefficient is reversed at the position where the phase mismatch is accumulated to π (this is also called coherent length). Thus, the electric field of the new frequency will continue to grow.

Compared to the birefringent phase match, it 1) can utilize the largest elements of the nonlinear tensor since it does not require two different polarization states of the involved waves; 2) does not have the spatial walk-off problem. This allows the laser to be intensely focused on the crystal and the nonlinear interactions in waveguides; 3) can use realized in any material which has weak or no birefringence. 4) has a period that can be adjusted to obtain phase matching at room temperature or any convenient temperature. The limitations of QPM are 1) the fabrication process is highly dependent on the material. Currently, only certain QPM crystals are available; 2) the thickness of the QPM structure is limited. It cannot be used in a high-power laser with a very large beam waist.

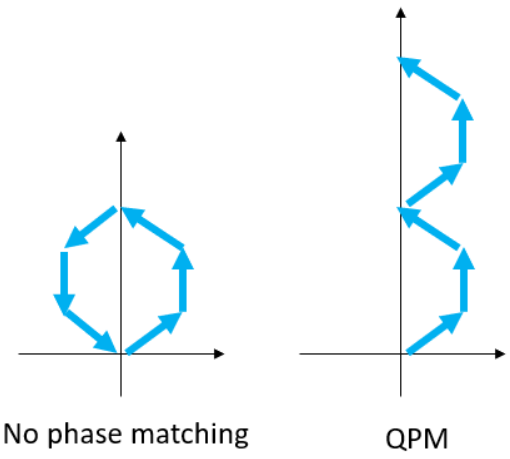

Figure 1: The construction of the amplitude in no phase matching crystal and QPM crystal.

As shown in Figure 1, in the no phase match crystal, the amplitude will revert to zero after two coherent lengths. The amplitude in the QPM crystal will continue growing. The QPM crystal has a lower conversion efficiency compared to the perfectly phase matching. The effective nonlinear coefficient $d_{eff}$for the QPM crystal is $d_{eff}(2/\pi)$. However, juxtaposed to the birefringent phase matching, QPM usually possesses a high conversion efficiency because it can use a higher nonlinear coefficient in the nonlinear tensor as a result of its possibility to use the same polarization direction for all interaction waves. QPM is now widely used for frequency doubling and for parametric devices such as optical parametric oscillators.

In the OPOs we build in our lab, the crystal was placed at Brewster's angle. The $\bar{4}$3m orientation patterned crystal was cut such that the light in the crystal was perpendicular to the walls of the periodical structure and the polarization of the light is along the <111> direction. The cutting of the OP-GaAs was illustrated in Figure 2.

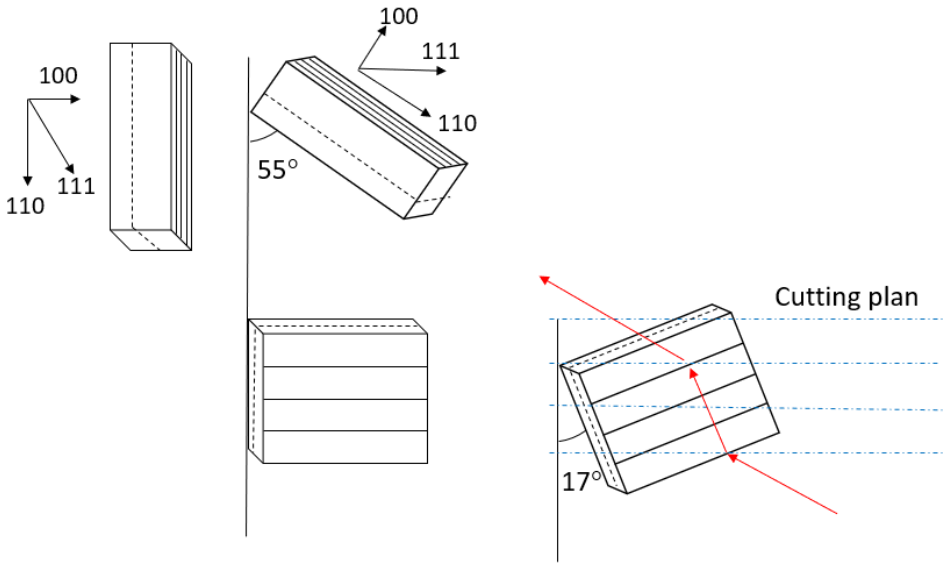

Figure 2: Orientation pattered $\bar{4}$3m crystal (OP-GaAs, OP-GaP) prepared for cutting showing the relative orientations of the crystallographic planes, poled domains and cutting planes.

2.4 Lock cavity length of the OPO

In the subharmonic OPO, the signal and idler are doubly resonating. The oscillation is interferometrically sensitive to the cavity length. The consecutive oscillations are separated by a half the degenerate wavelength (or the wavelength of the pump wave). For each oscillation peak, the cavity length needs to be stabilized to sub 100 nm range to achieve a stable spectrum shape.

To stabilize the OPO cavity length, the dithering-lock method was used on the OPO. Since the frequency of the OPO is intrinsically locked to the OPO regardless of any change to the cavity length, it cannot be used as feedback to stabilize the OPO's cavity length. However, the outpower power varies as the cavity length changes, which makes it suitable for working as a feedback signal to stabilize the cavity length. Since the OPO needs to be stabilized at the top of the intensity, we need to add a small dithering signal to the cavity length and take the derivative of the intensity signal vs cavity length to get a linear change as the feedback. However, this dithering lock method does not work well when the broadest spectrum is not corresponding to the highest output power or when the curve of the output power versus the cavity length has a flat top or more than one maximum points (shown in Figure 3a). This is a result of the detector collecting the power at all frequency components, which has a maximum at different cavity lengths.

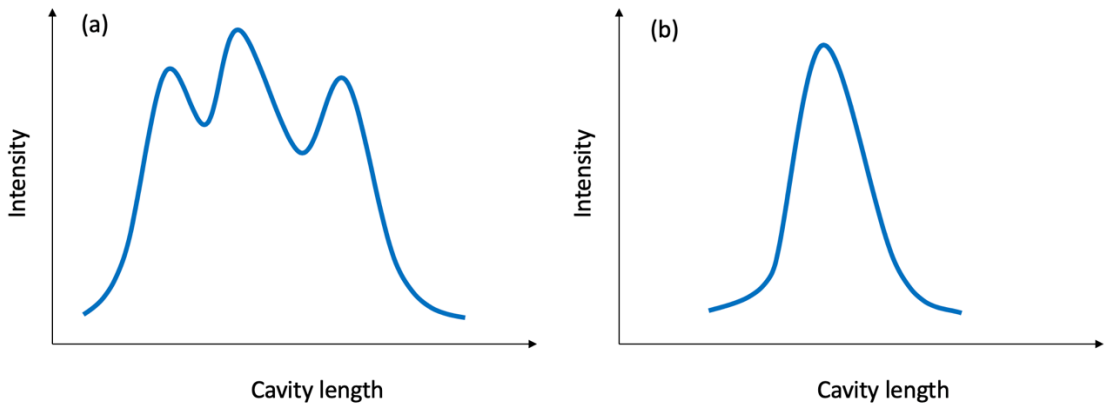

Figure 3: (a) The output intensity varies as the cavity length is detuned. (b) The intensity of the narrow bandwidth signal varies as the cavity length is detuned.

However, if we can use a bandpass filter to reduce the bandwidth of the output signal, the signal should have only one maximum intensity as shown in Figure 3b. A diffraction grating will separate the different frequency components of the output beam into different angle. The iris of the detector can work as a bandpass filter. One exciting feature of this method is that the intensity peaks for different frequency components are corresponding to the different cavity lengths. This means that one can easily select the desired cavity length by simply changing the location of the detector or the angle of the grating.

Moreover, we innovatively used two detectors to collect the signals at the different spectrum components of the output of the OPO (shown in Figure 4a). Then we obtained the signals with a single maximum at different cavity lengths as shown in Figure 4b. We can use the electric circuit to subtract the two signals to allow the linear signal to cover a longer cavity length (Figure 5). The linear signal can directly work as feedback to control the cavity length of the OPO.

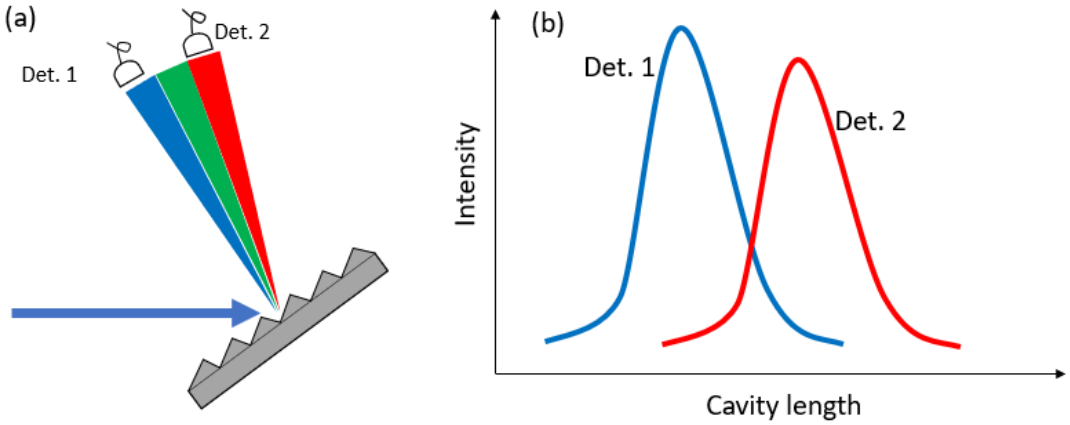

Figure 4: (a) The two detectors after the diffraction grating detect different frequency component of the output of the OPO. (2) the signals detected by detector 1 and 2.

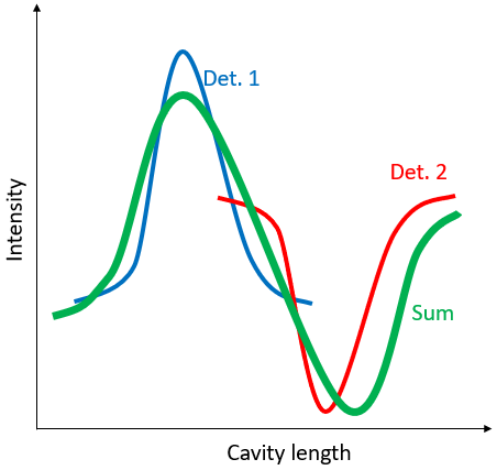

Figure 5: The signal for detect 1, detector 2 and the sum of the two signals. The sum signal could be directly used as the error signal to control the OPO cavity length without extra dithering signal.

2.5 Calibration of the spectrometer using black body radiation

The system we used to measure the 2D colored spectra consisted of a monochromator and an MCT detector. They do not have flat spectral response. To obtain the real spectrum shape, we need to calibrate the measurement system. Instead of measuring the spectral response of each instrument in the measurement system, we are going to calibrate the system as a whole.

The black body radiation has well-known spectral power distribution and could be used as the source for the calibration. In the experiment, we chose a 1000 °C Silicon carbide (SiC) as the light source to characterize the monochromator. The SiC source is manufactured by Newport with a model No. 80007. It is a complete SiC infrared light source and provides a smooth continuum from 700 t0 6000 cm^{-1} (1.7 to 14 μm). The MCT detector was cooled by liquid nitrogen to 77K.

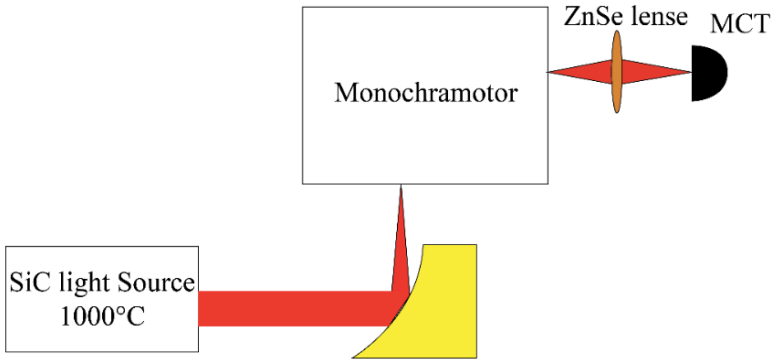

Figure 6: The experiment setup for calibrating the spectral measurement system.

To overcome the limitation of the free spectrum range of the diffraction gratings inside the monochromator, three long pass filters (cutoff wavelength at 2.5 μm, 4.5 μm and 7.4 μm) were used to measure the spectrum in different ranges. By comparing the black body spectrum curve with the acquired spectrum, the transmit coefficient of the system can be calculated. The coefficient will include all the components in the spectrum measurement system, such as the focus lenses, the diffraction gratings, and the MCT detector. The gratings in the monochromator have a groove density of 100 lines/mm is blazed at 6 μm. The data we measured is shown in Figure 7.

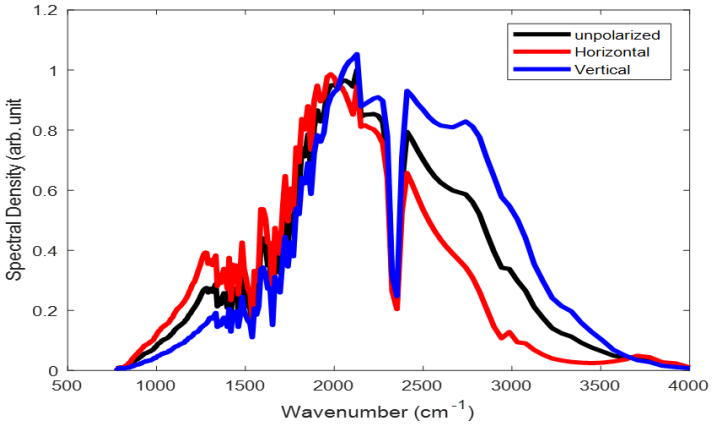

Figure 7: The measured spectrum of the SiC (1000 °C) for unpolarized light (black curve), horizontal polarized light (red curve), and the vertical polarized light (red curve).

The measured spectrum divided by the spectrum of the SiC source give us a spectral coefficient for transmission. The measurement system is not purged except in the monochromator. The dips in the relative efficiency are due to the absorption of water vapor and carbon dioxide in the measurement system.

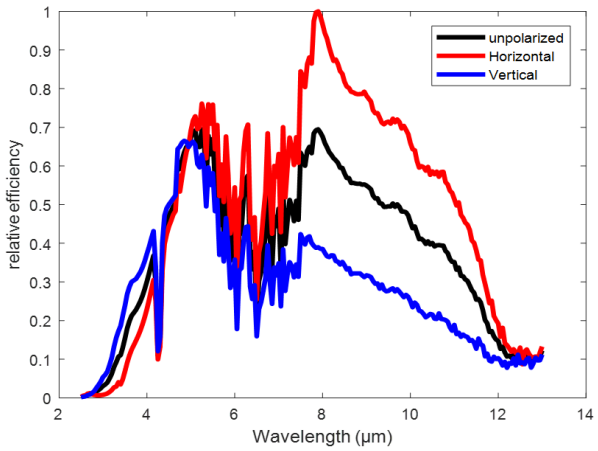

Figure 8: The calibrated spectrum for the 100 lines/mm grating blazed at 6 μm.

The measured coefficient could be used to calibrate the spectrum measured by the monochromator plus MCT detector, to get the real spectrum.

CHAPTER THREE: OP-GaAs OPO PUMPED BY A Cr^{2+}:ZnS LASER

3.1 Cr^{2+}:ZnS Pump Laser

Transition-metal-doped II-VI semiconductors, such as Cr^{2+} and Fe^{2+} doped ZnS and ZnSe, are suitable for high-power mid-IR lasing [36-39]: 1) a four-level energy 2) an absence of excited state absorption 3) close to 100% quantum efficiency of florescence (Cr^{2+} only) 4) broad vibronic absorption and emission band. Cr:ZnS and Cr:ZnSe laser can be pumped by reliable erbium and thulium fiber lasers. In 2016, Sergey Vasilyev et al. demonstrated the 1.7 W output Kerr-lens mode-locked master oscillator at a 2.4 μm central wavelength. The output was further amplified to 7.1 W with 450 nm bandwidth at -3 dB level [38].

The schematic Cr^{2+}:ZnS laser structure is shown in Figure 9. The X-folded standing-wave resonator consists of two concave mirrors, plane-end mirrors, and plane folding mirrors. The laser was pumped by a 1567 nm linear polarized Er-doped fiber laser. The pump beam is focused in the gain element by a lens and coupled into the resonator through a curved mirror with high reflectivity in the 2200-2700 nm range and high transmission at the pump wavelength. The outcoupler for the 2.35 μm is a ZnSe wedge, with 90% (0.8W) or 70% (1.2W) outcoupling. The SHG is outcoupled thought a curved dichroic mirror, which highly reflects the mid-IR wave and highly transmits 1100-1350 nm.

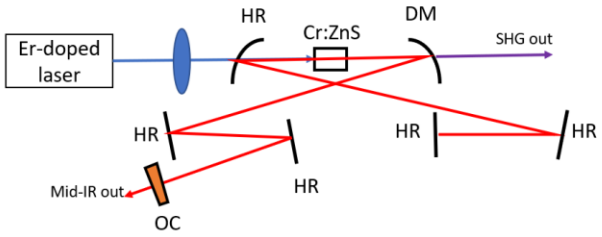

Figure 9: The schematic of the Cr^{2+}:ZnS laser. DM: dichroic mirror. HR: high reflection mirror. OC: output coupler.

3.2 OP-GaAs OPO

In the quest for obtaining a broad spectrum, we first looked to using an OP-GaAs based OPO. The OP-GaAs features broad transparency 0.9 – 17 μm in the mid-infrared region and higher nonlinearity than PPLN [40]. These characteristics make it an ideal nonlinear crystal for expanding the near-infrared comb to the mid-infrared region using a nonlinear process. Moreover, the relatively low group velocity dispersion (GVD) of GaAs in the mid-infrared region (GVD = 0 at 6.6 μm) enables producing a broadband spectrum in the subharmonic OPO. A spectrum extending from 2.6 to 6.1 μm at the -30 dB level has been demonstrated in a OP-GaAs OPO pumped by a Tm-fiber laser in 2012 [24].

The ring-cavity of the OP-GaAs based OPO was synchronously pumped by a free running Kerr-lens mode-locked 2.35 μm Cr^{2+}:ZnS laser, with 62-fs time-bandwidth limited pulse duration average power, and a 79 MHz repetition rate. The OPO cavity (Figure 10) was composed of two gold-coated parabolic mirrors (M1 and M2) with a 30° off-axis angle and apex radius 30 mm, five flat gold-coated mirrors (for simplicity only M3 was shown in the setup figure, the other four gold mirrors were simply used for folding the cavity), and a dielectric mirror M4 (YAG substitute) with a high reflection (>90%) for 2.6-7.2 μm (except dips at 2.8 and 3.1 μm) or midrate reflection

(>50%) for 2.8-8 μm and high transmission (>90%) for the 2.35-μm pump. A 0.3-mm-thick ZnSe wedge was used inside the cavity to minimize group velocity dispersion and for outcoupling the signal/idler wave.

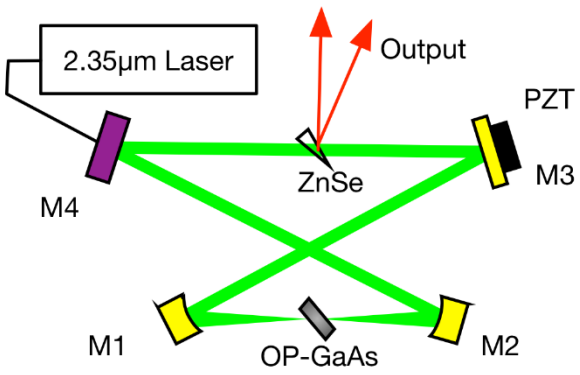

Figure 10: The experimental setup of the 2.35-μm Cr^{2+}:ZnS laser pumped OP-GaAs OPO. M1 and M2 are parabolic gold-coated mirrors, M3 is a flat gold-coated mirror, and M4 is the dielectric incoupling mirror. The ZnSe wedge was used for dispersion compensation and outcoupling the signal/idler wave. PZT is the piezo attached to the mirror for fine-tuning the cavity length.

The 0.5-mm-long GaAs was made at BAE Systems by a combination of molecular-beam and hydride vapor phase epitaxy [41]. The GaAs was placed at a Brewster angle and its QPM period of GaAs was 88 μm, designed to get the broadest parametric gain at OPO degeneracy. All polarizations were along the <111> direction of the GaAs crystal to get the maximum nonlinear coefficient. Usually the normalized parametric gain of QMP-nonlinear crystal was calculated by assuming the pump was monochromatic. However, in the femtosecond laser pumped OPO, the pump wavelength has a broad bandwidth. Here, the relative normalized parametric gain of 0.5-mm OP-GaAs was calculated when the pump has FWHM 90-nm bandwidth around 2350 nm, corresponding to our experiment (Figure 11). The calculated FWHM gain bandwidth for

subharmonic generation is from 3.3 to 8 μm. The real spectrum can be broader than this due to the difference frequency generation between the side frequency of the pump wave and the OPO signal/idler wave.

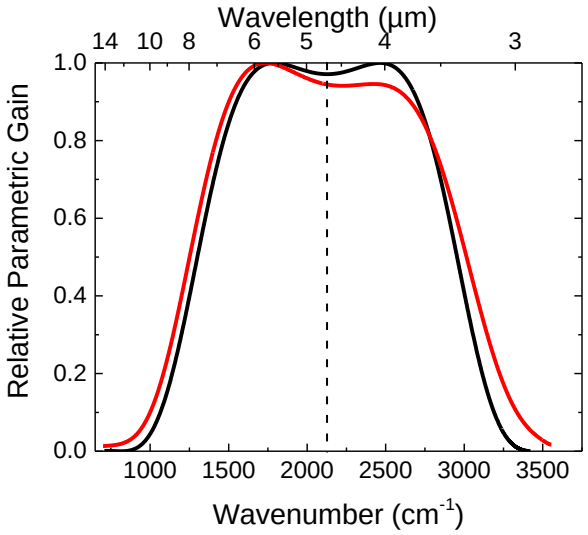

Figure 11: The relative parametric gain for 0.5-mm thick 88-μm QPM period OP-GaAs. The black curve corresponds to a monochromatic 2.35 μm pump, while the red curve takes into account the real spectrum of the fs pump pulse.

A low pump threshold 8 mW was achieved in the OP-GaAs OPO, as a result of the double resonance and ultra-short pump pulse duration. The low pump threshold the degenerate OPO aids it in achieving the broad bandwidth spectrum.

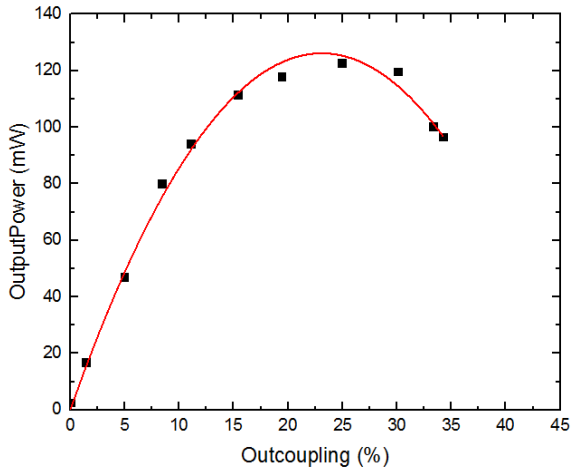

Figure 12: The output power vs. the outcoupling. The red curve is the 2nd order fitted polynomial curve. The maximum output power 122 mW was achieved around 25% outcoupling.

The output power versus the outcoupling was measured by rotating the ZnSe paralleled plate in the cavity (Figure 12). The maximum output power from the ZnSe plate was 122 mW when the outcoupling was 25% (when we measured the power, we took into account the fact that a long pass filter placed before the power meter had 90% transmission).

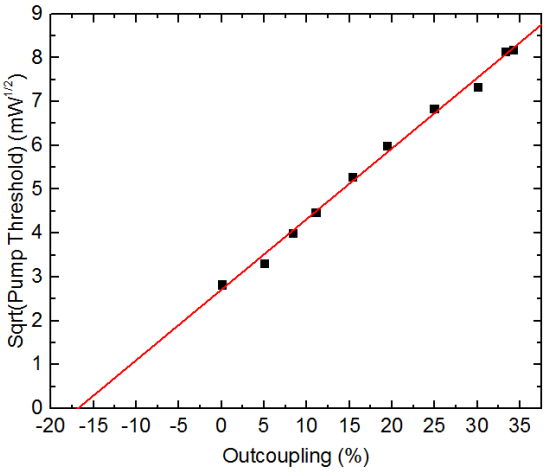

Figure 13: square root of the pump threshold versus the outcoupling. The red fitting line indicate the intra-cavity loss was 17% (originating from the 10% loss on the dielectric incoupling mirror and imperfect reflection of the gold mirrors).

For a doubly resonant OPO, the threshold scales as the square of the total intra-cavity loss, which is confirmed by the linear dependence in Figure 13, where the vertical axis is the square root of the pump threshold and the horizontal axis is the outcoupling of an ZnSe parallel plate. By extending the fitting line to cross the horizontal axis, we found that the intra-cavity loss was 17%, (~10% percent comes from the dielectric incoupling mirror, and the rest – from reflection loss of the gold mirrors in the OPO cavity).

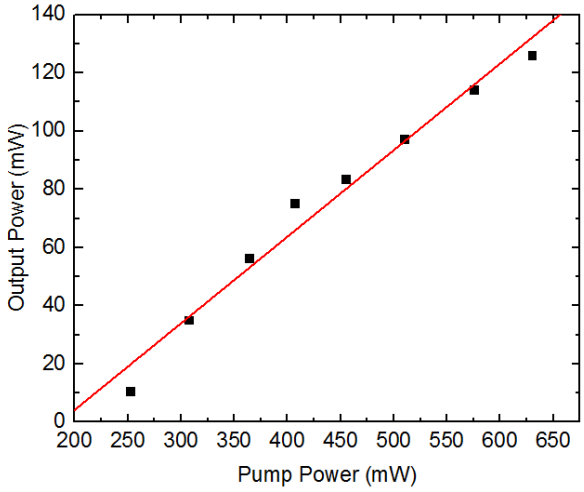

Figure 14: Output power versus the pump power. The pump slope efficiency was 30%. No roll-off was observed at maximum pump power.

With 25% outcoupling efficiency, the output power versus the input power characteristic was measured (Figure 14). The pump slope efficiency was 30%. No output roll-off was observed at the maximum pump power 630 mW. This observation signifies that the three-photon absorption of the 2.35 μm absorption and other unwanted high-order effects play a minor role.

Dispersion is a key element affecting the spectrum width of the OPO. In the synchronously pumped OPO, the signal/idler pulse needs to be temporally overlapped with the pump pulse to achieve

sufficient gain. A flat group delay would enable more wavelengths to acquire enough gain and overcome the loss to start oscillating. Around 4.7 μm, the dielectric incoupling mirror has a negative GDD (group delay dispersion) -500 fs^2, which adds a quadratic extra phase (by integrating the GDD twice) to the signal/idler wave per cavity round trip (black curve in Figure 15). The extra phase due to the 0.5-mm OP-GaAs was also computed in the green curve of Figure 15. A 0.3-mm thick ZnSe wedge was placed in the OPO cavity to work as an outcoupler and further reduce the dispersion around 4.7 μm. Taking all the dispersion elements in the cavity into account, the total extra phase was in the estimated tolerance ±0.5 rad from 1400 to 3000 cm^{-1} (3.3 to 7.1 μm).

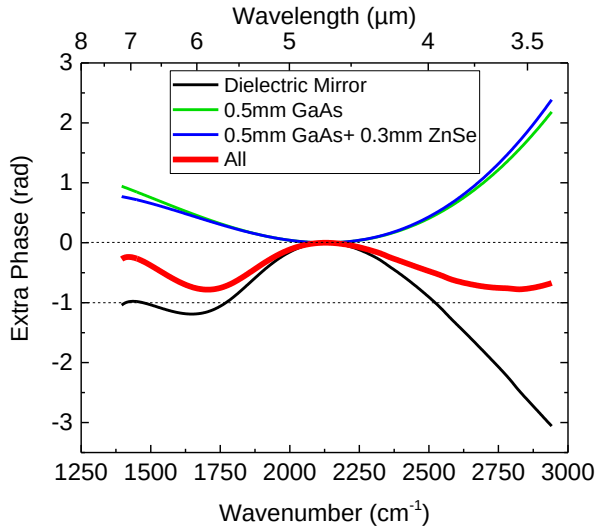

Figure 15: The computed cavity extra phase accumulated per round trip. The horizontal dashed lines indicate the estimated tolerance ± 0.5 rad. Red curve: all the elements in the cavity. Black curve: the dielectric incoupling mirror. Green curve: 0.5-mm OP-GaAs crystal. Blue curve: 0.5-mm OP-GaAs crystal and 0.3-mm ZnSe wedge.

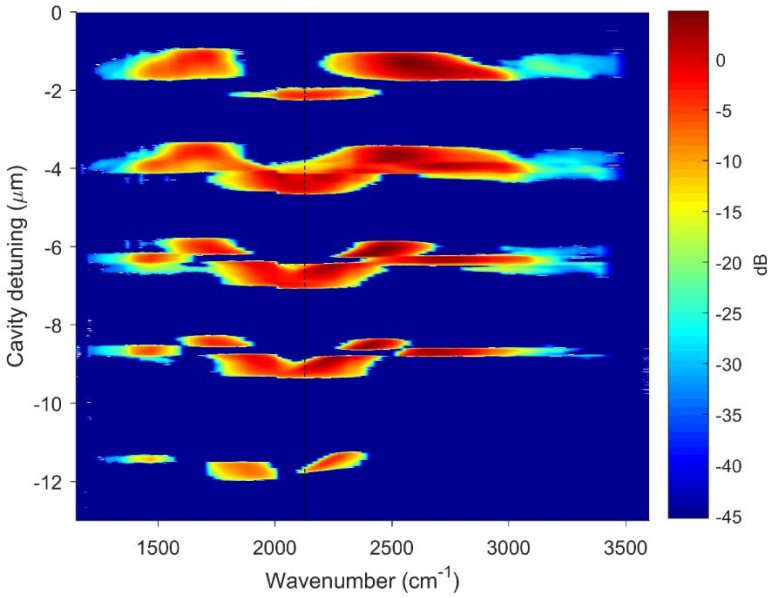

Figure 16: The 2D spectra measured by detuning the cavity length in steps, corresponding to integer of the pump wavelength (2.35 μm). The dashed line indicates the degenerate frequency 2127 cm-1 (4.7 μm).

Because of double (signal and idler) resonance, the OPO works at several discrete cavity lengths with a separation of 2.35 μm (the pump wavelength) when the piezo actuator detunes the cavity. When transitioning from the longer to the shorter cavity, the output spectrum varies gradually (Figure 16) due to the change of effective dispersion. The second peak from the top yields an extremely broad spectrum extending from 1190 to 3500 cm^{-1} (2.85 - 8.40 μm) at -40 dB, more than 1.5 octaves in the frequency band. The usual (1D) spectrum corresponding to this peak is shown in Figure 17. This wavelength range covers the characteristic spectrum of numerous molecules, such as CH_4, SO_2, CO_2, CO, COS, N_2O, NO and etc. The blue dotted curve in Figure 17 is the reflectivity of the dielectric in-coupling mirror.

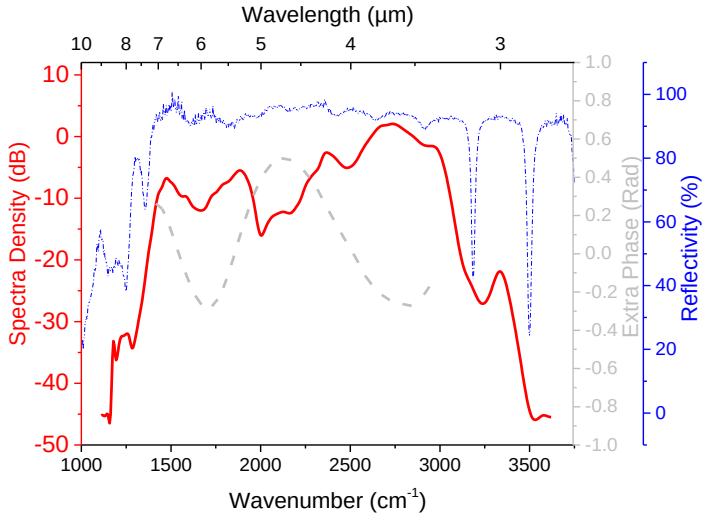

Figure 17: Red curve: 1D spectrum corresponding to the second peak in the 2D spectrum. Dashed gray: the computed cavity extra phase accumulated per round trip. Dash dot: reflectivity of the dielectric incoupling mirror.

The dielectric mirror has a broad reflection bandwidth from 2.9-8 μm (>50%), and two dips at 3.1 and 2.8 μm. The latter features correlate with the OPO output spectrum. A dielectric mirror with such a broad reflection bandwidth has thick coating layers, which introduce large GDD (-500 fs^2 at 4.7 μm, the OPO degenerate wavelength). We believe the reflectivity and dispersion of the dielectric mirror is the main limitation for getting an even broader spectrum. In the future, we will use a dielectric incoupling mirror with a broader reflection bandwidth and lower GDD to further extend the output bandwidth.

In conclusion, we achieved 122 mW of average power from the subharmonic OP-GaAs OPO pumped by the ultrafast Cr^{2+}:ZnS laser [42]. The pump slope efficiency was 30%. No roll-off was observed, which indicates that the OPO output power can be further increased by simply increasing the pump power. By optimizing the OPO cavity, the OPO can still work when the pump power

was as low as 8 mW. The observed 85% pump depletion indicates that most of the pump can be converted into the broadband OPO subharmonic, provided that an appropriate outcoupling is used. The instantaneous spectral span of 2.85 - 8.40 μm (1.56 octaves) achieved from this OPO can serve as the basis for a fully stabilized frequency comb in the mid-IR molecular 'signature' region. The spectrum can be further broadened by fabricating an incoupling dielectric mirror with (i) broader reflectivity range and (ii) with compensation of the residual group velocity dispersion.

3.3 GHz OP-GaAs OPO

Applying the frequency combs in nonlinear comb spectroscopy requires high power per mode, which could be achieved using high repetition rate frequency combs without increasing the average power.

Higher repetition rate frequency combs have large mode spacing corresponding to higher power per mode. They can provide higher signal-to-noise ratio when applied to the spectroscopy and frequency metrology [43]. They enable the use of lower resolution spectral dispersers when applied to the optical arbitrary wave generation.

The OPO cavity was a bowtie shaped ring cavity. Since the repetition rate is 11 times higher, the cavity length is reduced to 34 cm to match the 0.9 GHz repetition rate of the pump laser. The pump beam was incoupled into the OPO through a pumped incoupling mirror, which higly reflects the pump beam (2.35 μm) and highly transmits the mid-infrared wave (3.5 – 7 μm). A pair of gold coated parabolic mirrors was used to focus the pump beam on the OP-GaAs crystal. The OP-GaAs crystal had an orientation period of $\Lambda = 88$ μm. The OP-GaAs crystal was grown by a combination of molecular beam epitaxy and hydride vapor phase epitaxy at BAE systems. The crystal was

mounted at the Brewster's angle (73.1°) to minimize the reflection loss of the p-polarized light at 4.7 μm and forces the light oscillating in the cavity to be along the <111> direction.

A ZnSe wedge with a 1° apex angle was inserted in the cavity to 1) outcouple the mid-infrared beam and 2) compensate the cavity dispersion. The outcoupling ratio was controlled by tilting the ZnSe wedge to a different angle. The thickness of the ZnSe in the cavity could be used to balance the group delay dispersion and the group velocity dispersion to match the CEO frequency of the pump laser. One challenge for the 0.9 GHz OPO to function is the lower energy per pulse. The pulse energy for this laser is 8 nJ, which is equivalent to an 80 MHz laser with 0.64 W average power.

The OPO was covered by a Plexiglass box and purged by nitrogen to reduce the absorption caused by water and carbon dioxide. The overall footprint of the OPO setup was about 1 m^2, but only ~0.06 m^2 was used for the OPO cavity. The other space was used for the optical path of mode matching.

Since this OPO was a doubly resonant OPO, it was interferometrically sensitive to the cavity length. It oscillates at different cavity lengths in a step like fashion. (Figure 18)

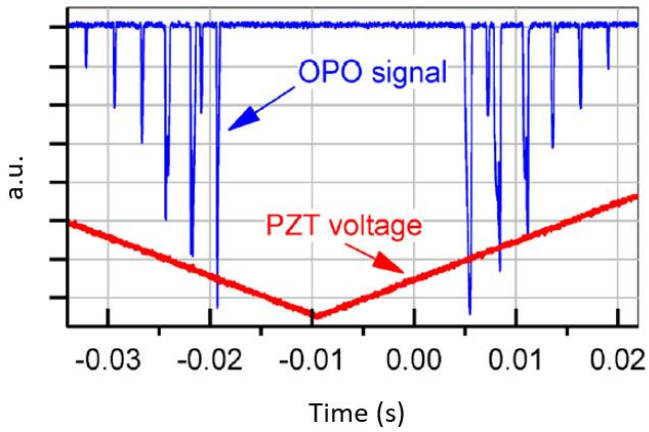

Figure 18: Detected OPO peaks (inverted) vs. time. The length of the OPO resonator is scanned at 10 Hz rate by a piezo transducer. The consecutive peaks of the OPO are separated by half of the degenerate wavelength (2.35 μm) in terms of the cavity round trip change.

The pump threshold was measured to be 162 mW by tilting the ZnSe outcoupling wedge at the Brewster's angle to make the outcoupling ratio close to zero. The pumped depletion was measured using the residual beam outcoupled through the pump incoupling mirror.

The spectrum of the OPO was measured by a monochromator and MCT detector (cooled to 77K). The spectrum varies at different cavity lengths. By putting all the spectra corresponding to all cavity lengths in a single figure, we could better understand how the spectrum evolves when detuning the cavity length (Figure 19). More than 5 oscillation peaks were observed in the experiment.

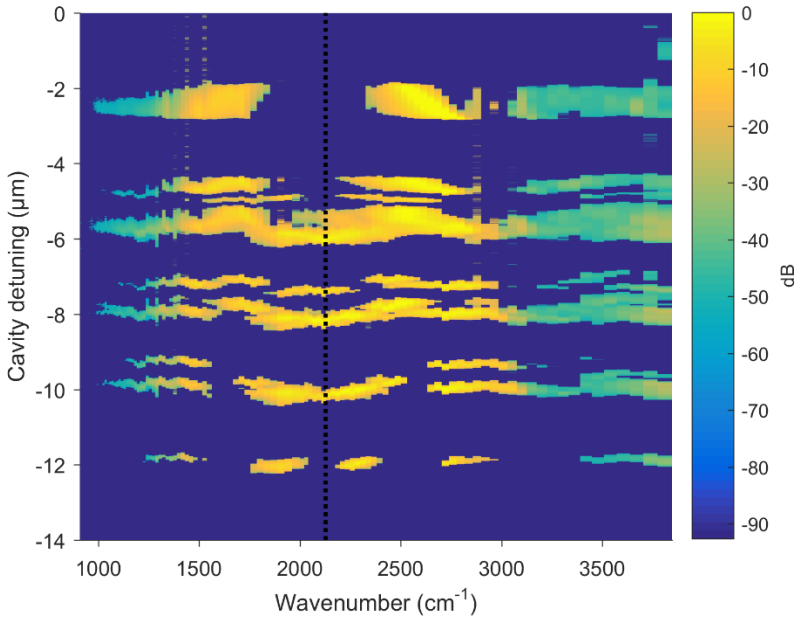

Figure 19: The 2D colored spectrum of the 0.9 GHz OPO. The dotted black line indicates the degenerate wavelength of the OPO. The broadest degenerate spectrum is corresponding to the second oscillation peak.

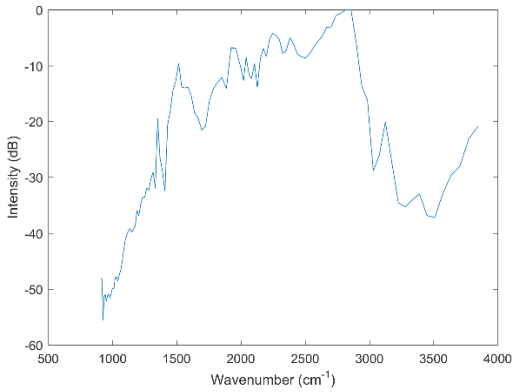

Figure 20: The broad 1D spectrum achieved corresponding to 1 slice in the 2D color spectra.

In conclusion, a compact high-power MIR infrared source was demonstrated which works at 0.9 GHz and yielded a more than one octave spectrum (3 – 8 m). A 2.6% conversion efficiency from Er-doped fiber laser to broadband mid-infrared wave was achieved.

CHAPTER FOUR: OP-GaP OPO PUMPED BY NEAR- AND MID-INFRARED LASERS

4.1 Orientation-patterned GaP

The next material we utilized on our broadband spectrum journey was orientation-patterned gallium phosphide (OP-GaP). OP-GaP is a new QPM nonlinear material with excellent transmission in the mid-IR (longwave cutoff at ~13 μm). In 2015, the first OP-GaP based OPO was demonstrated pumped by a 2-μm nanosecond laser [44]. Recently, femtosecond OPOs based on OP-GaP, with pump wavelengths near 1 μm [45], and 2 μm [46], were demonstrated.

GaP has an indirect band gap of 2.26 eV (0.55 μm) and a nonlinear coefficient of d_{14}=35 pm/V. It is smaller than that of GaAs (d_{14}=96 pm/V), however, considering the fact that GaAs has a noticeable multi-photon (including 2-, 3- and 4-photon) absorption [47, 48] when pumped between 1.5 and 2.5 μm, GaP has an advantage of having much smaller multi-photon absorption in this range. In addition, GaP has a significant advantage during the HPVE [49]. OP-GaAs will gradually degrade the duty cycle with increasing thickness, and the domain walls always exhibit a small 1° taper, whereas the domain walls in the OP-GaP remain perfectly parallel throughout the growth process.

OP-GaP has a broader transparency compared to periodically poled lithium niobate (PPLN) (0.4 – 5 μm). The absolute value of GVD for GaP at 3.1 μm is 281 fs^2/mm which is more than two-fold smaller than the PPLN (-697 fs^2/mm). This small dispersion is a prerequisite of the broadband output spectrum.

An additional advantage of using OP-GaP in a subharmonic OPO in combination with an ultrafast 2.35-μm pump is that the GaP crystal has a negligible second-order dispersion near degeneracy (the zero crossing is at 4.8 μm). Here we demonstrate more than two-octaves-wide spectrum (3 – 12.5 μm) from a subharmonic OPO based on OP-GaP pumped by a 2.35 μm femtosecond laser.

4.2 OP-GaP OPO Pumped by 1.5μm

The OP-GaP based OPO is pumped by a telecommunication-range fiber laser and is suitable for producing phase-locked frequency combs in the mid-IR. A schematic of the OPO setup is presented in Figure 21. The pump source was an Er-doped fiber laser from Toptica Inc. (1560-nm central wavelength, 300-mW average power, 80-MHz repetition frequency and 85-fs pulse duration). We regard this laser as a free running frequency comb in this work. The compact OPO cavity was composed of a dielectric pump incoupling mirror (M1) with a high transmission (>85%) at 1560 nm and high reflection for the signal/idler wavelengths (>95% at 2.4-4.2 μm and > 50% at 2.2-4.9 μm) and three gold-coated mirrors (M2-M4), two of which (M2 and M3) are parabolic with an off-axis angle of 30° and radius curvature in the apex R=30 mm, and one of which (M3) was flat (not shown are 4 gold-coated folding mirrors to reduce the footprint). A broad-bandwidth gain was provided by a 0.5-mm thick OP-GaP crystal, with a QPM period 46.5 μm, grown by a combination of molecular beam epitaxy (MBE) and low-pressure hydride vapor phase epitaxy (HVPE). The OP-GaP crystal was mounted at the Brewster's angle (71°), to minimize the reflection of the p-polarized signal/idler and pump waves. Inside the crystal, the beams propagated along <-110> and all polarizations were along <111> direction of GaP.

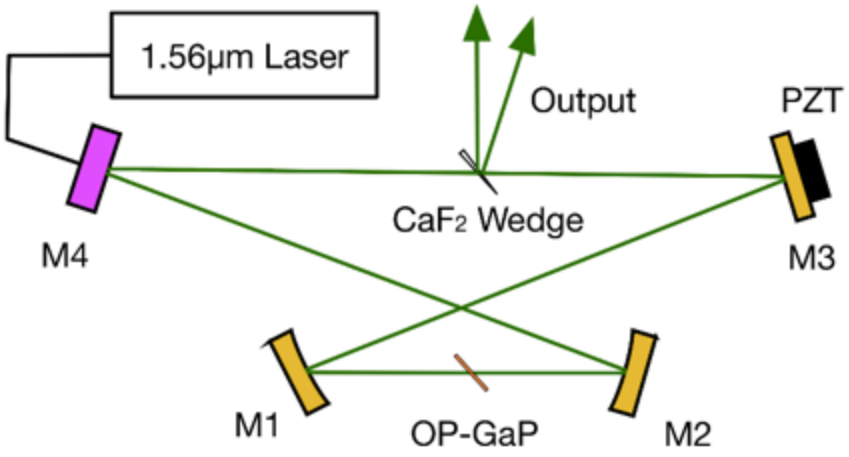

Figure 21: The OPO schematic. M1 is a dielectric mirror which highly transmits the pump wave and highly reflects the signal/idler wave of the OPO. The M2 and M3 are parabolic gold-coated mirrors, M4 is a flat gold-coated mirror with a piezoelectric transducer (PZT) for cavity length tuning.

A CaF2 wedge (1° angle, average thickness 1.14 mm) was placed in the cavity to (i) compensate, in the first-order approximation, the GVD of GaP (at 3.12-μm degeneracy, GaP has GVD of 280 fs2/mm and CaF2 has -122 fs2/mm) and (ii) for the OPO beam outcoupling via Fresnel reflection.

Figure 22 shows the computed overall extra phase delay accumulated per OPO cavity round-trip, as a function of frequency, along with contributions of the GaP crystal, CaF_2 wedge, and dielectric mirror. (The extra phase is the result of the residual group velocity dispersion that causes resonator modes to be slightly non-equidistant. This causes an extra phase accumulated per roundtrip for each mode. The latter is calculated via double integration, over frequency, of the roundtrip group delay dispersion, expressed in fs^2). Our estimate for the extra phase tolerance is ± 0.5 rad, which comes from the finesse of the cavity and the available pump power. From the Figure 22 one can see that the computed overall round-trip extra phase allows for a spectrum more than one octave-wide to be achieved.

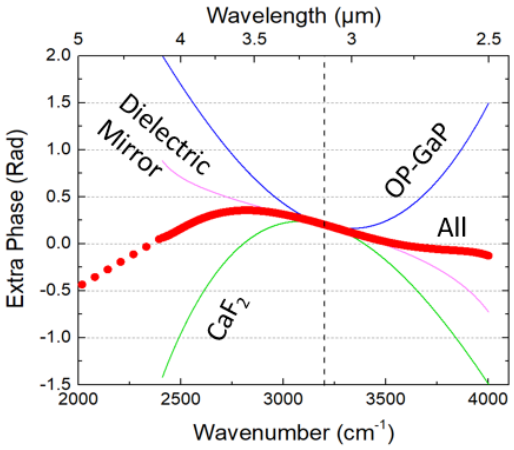

Figure 22: The computed extra phase per OPO cavity round-trip, as a function of frequency (thick line), along with contribution of the GaP crystal, CaF_2 wedge, and dielectric mirror.

Usually, parametric gain of a nonlinear crystal is calculated by assuming a monochromatic pump. Here we calculated parametric gain by assuming a finite (~100 nm) full-width half-maximum (FWHM) Gaussian spectrum of the pump. The corresponding parametric gain for the 0.5-mm thick OP-GaP used in our OPO is shown as a thick red line in Figure 23, where one can see that the FWHM gain bandwidth is from 2070 to 4370 cm^{-1} (2.28 - 4.83 μm). The gain curve for a monochromatic pump is also plotted on the same figure for comparison.

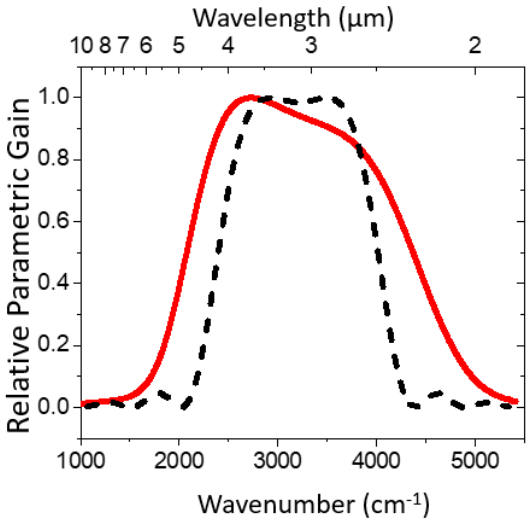

Figure 23: The relative parametric gain for the finite pump spectrum (solid line) as compared to that for the monochromatic pump spectrum (dashed black)

The OPO oscillation was achieved by tuning the cavity length using a piezo actuator attached to the mirror M4. The OPO pump threshold was measured to be 14 mW. This low threshold is a result of a doubly-resonant performance [50]. Figure 24 shows the output power vs. outcoupling from the CaF2 wedge, which was varied by turning the wedge away from the Brewster angle towards normal. The highest mid-IR power (sum of two reflections from CaF2 surfaces) of 29 mW was achieved at ~ 17% outcoupling. The measured OPO pump depletion was 75%.

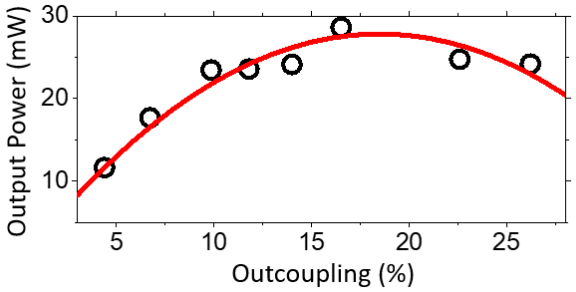

Figure 24: The OPO output power from two surfaces of the CaF_2 wedge versus outcoupling strength. The solid curve is a trace for the eye.

A doubly resonant OPO oscillates at several discrete cavity lengths (that are close to the synchronous pumping condition), separated in roundtrip by the wavelength of the pump (1.56 μm) [23]. Switching from one resonant cavity length to another is equivalent to changing, in a step like fashion, the dispersion in the cavity, which results in the change of the instantaneous spectrum. The OPO output spectrum was measured using a monochromator and a HgCdTe detector. The 2D color-coded intensity plots of Figure 25 represent the output spectra as a function of cavity length detuning. Each horizontal 'stripe' corresponds to one of the resonant peaks in the OPO output. The OPO spectrum evolved from degenerate to nondegenerate mode when the cavity was detuned to shorter lengths. The second stripe from the top yields the broadest instantaneous spectrum while still being degenerate.

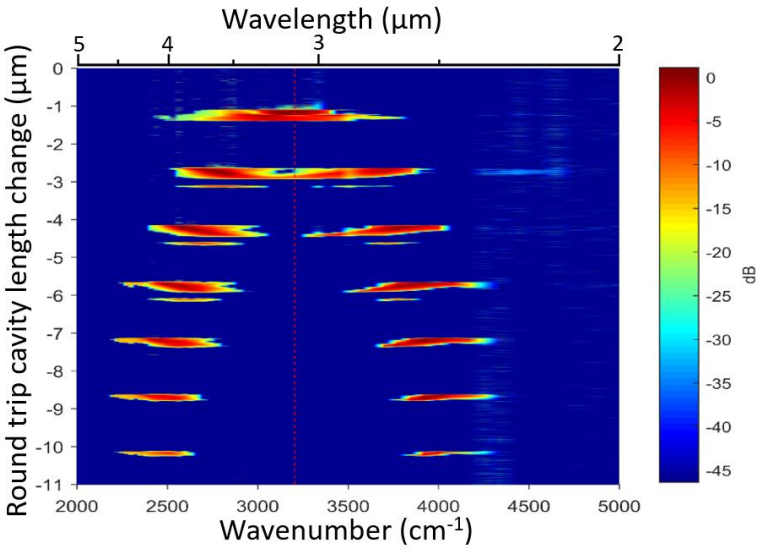

Figure 25: 2D color intensity plots of the output spectra as the resonator length is detuned.

Continuous operation of the OPO was achieved by locking the cavity length to one of the resonances via dither-and-lock method [23] involving a PZT actuator and a lock-box (LaseLock from TEM-Messtechnik GmbH). Figure 26 shows the broadest measured degenerate OPO spectrum spanning from 2.30 to 4.84 µm (2064-4346 cm^{-1}) at -25 dB level. This spectrum corresponds to the second stripe from the top on the 2D plot of Figure 25. Although the cavity was purged with dry nitrogen which reduced the CO_2 concentration to less than 5 ppm and the H2O concentration to 400 ppm, the spectrum was still affected by the absorption of these two molecules in the measurement system. The top panel of Figure 26 shows the cavity roundtrip transmission, corresponding to the above concentrations, averaged over 10 cm^{-1} to match the resolution of the monochromator.

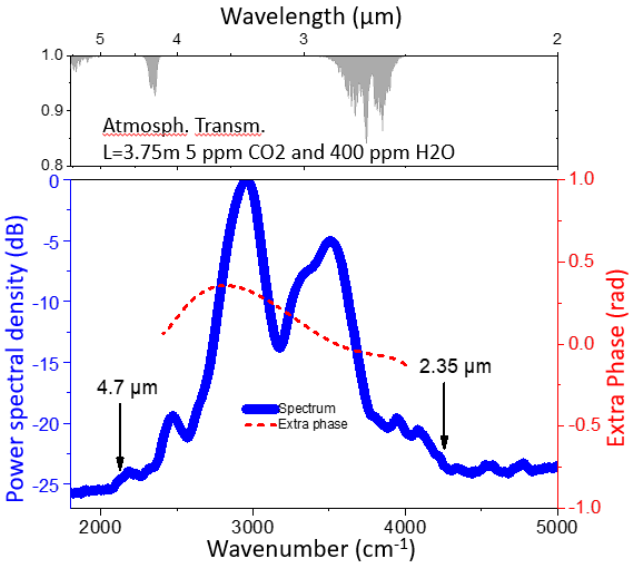

Figure 26: The broadest measured degenerate OPO spectrum (solid line). Also shown is the calculated round-trip cavity extra phase (dashed line). The top panel shows transmission for one cavity round-trip for 5 ppm CO_2 and 400 ppm H_2O.

Finally, the 2-nd order autocorrelation trace corresponding to the broadest spectrum of Figure 26 was measured with an InGaAs photodiode serving as a 2-photon detector and is shown in Figure 27. Also shown is the simulation trace assuming $sech^2$ shape and FWHM pulse duration of 70 fs. However, this duration is the upper limit, since the pulse was broadened by the dispersion of the optical elements used, such as a long-pass filter, beam splitter, and the focusing lens.

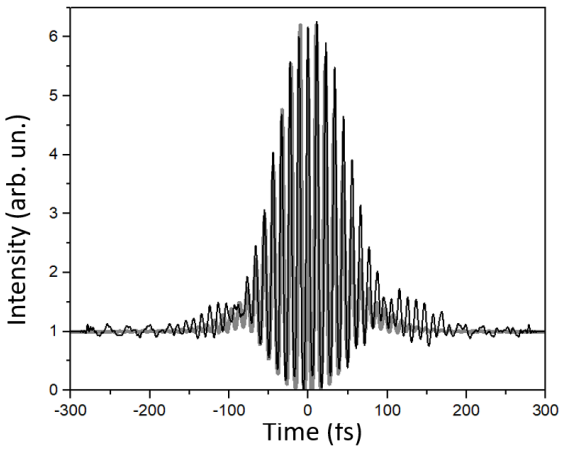

Figure 27: The 2-nd order interferometric autocorrelation trace (thin black). Simulated curve assuming sech^2 pulse with 70-fs FWHM (thick gray).

In conclusion, using an orientation-patterned GaP crystal as the gain element, we achieved an octave-wide 2.30 – 4.84 μm spectrum in a low-threshold (14-mW) subharmonic OPO, pumped by a free running Er-fiber laser comb [51]. The average comb output power was 29 mW. The spectral span achieved was more than 50% broader, as compared to the prior state-of-the-art based on an Er-fiber-pumped PPLN-based system.

4.3 Dispersionless OP-GaP OPO Pumped by 2.35 μm

Orientation-patterned gallium phosphide (OP-GaP) is a new QPM nonlinear material with excellent transmission in the mid-IR (longwave cutoff at ~13 μm). Recently, femtosecond OPOs based on OP-GaP, with pump wavelengths near 1 μm [45], 1.5 μm [51], and 2 μm [46], were demonstrated. GaP has an indirect band gap of 2.26 eV and a nonlinear coefficient of d_{14}=35 pm/V. It is smaller than that of GaAs (d_{14}=96 pm/V), however, considering the fact that GaAs has a noticeable multi-photon (including 2-, 3- and 4-photon) absorption when pumped between 1.5 and 2.5 μm, GaP has an advantage of having much smaller multi-photon absorption in this range. An additional advantage of using OP-GaP in a subharmonic OPO in combination with an ultrafast 2.35-μm pump is that the GaP crystal has a negligible second-order dispersion near degeneracy (the zero crossing is at 4.8 μm). Here we demonstrate a more than two-octaves-wide spectrum (3 – 12.5 μm) from a subharmonic OPO based on OP-GaP pumped by a 2.35 μm femtosecond laser.

A schematic of the OPO setup is presented in Figure 28. The pump source was a Cr^{2+}:ZnS laser (2.35-μm central wavelength, 1.2-W average power, 79-MHz repetition frequency, and 62-fs pulse duration). The compact OPO cavity was composed of a dielectric pump injector with a high reflection (>90%) at 2.35 μm and high transmission for the signal/idler wavelengths (>95% at 3.5-7 μm and >50% at 2.8-12 μm) and four gold-coated mirrors (M1–M4), two of which (M1 and M2) are parabolic with an off-axis angle of 30° and radius curvature in the apex R = 30 mm. The two other mirrors (M3 and M4) were flat (not shown are four gold-coated folding mirrors to reduce the footprint). The pump injector approach has a few benefits: 1) it greatly decreases the group delay dispersion typically introduced by a reflective broadband dielectric mirror; 2) the cavity could be built using only gold-coated mirrors, which provide high reflectivity in a broad wavelength range.

A 0.3-0.8 mm thick ZnSe wedge (1° angle) was placed in the cavity for (1) controlling cavity dispersion and (2) the OPO beam outcoupling via Fresnel reflection (at 60° angle of incidence we had 3.4% outcoupling in two beams).

A broad-bandwidth gain was provided by a 0.5-mm thick OP-GaP crystal, with a QPM period 110 μm, grown by a combination of molecular beam epitaxy (MBE) and low-pressure hydride vapor phase epitaxy. The OP-GaP crystal was mounted at the Brewster's angle (71°), to minimize the reflection of the p-polarized signal/idler and pump waves. Inside the crystal, the beams propagated along <−110>, and all polarizations were along the <111> direction of GaP.

Figure 29 shows the computed overall extra phase delay accumulated per OPO cavity round-trip, as a function of frequency, along with contributions of the GaP crystal, ZnSe wedge, and injector. The extra phase is the result of the residual group velocity dispersion that causes resonator modes to be slightly non-equidistant. This causes an extra phase accumulated per round trip for each mode. Our estimate for the extra phase tolerance is 0.5 rad, which originates from the finesse of the cavity and the available pump power. We calculated the OP-GaP parametric gain by assuming a finite (∼90 nm wide) spectrum of the pump. The corresponding gain for the 0.5-mm thick crystal is shown as a dotted black line in Figure 29.

With a 3.4% OPO outcoupling, the pump depletion was measured to be 83% at the pump threshold of 58.4 mW. When we stabilized the OPO cavity length to the degenerate mode, the average power (in two output beams) was around 31.3 mW (we did not optimize the outcoupling for achieving higher power). A doubly resonant OPO oscillates at several discrete cavity lengths (that are close to the synchronous pumping condition), separated in round trip by the wavelength of the pump

(2.35 μm). Switching from one resonant cavity length to another is equivalent to changing, in a step-like fashion, the dispersion in the cavity, which results in the change of the instantaneous spectrum. The OPO output spectrum was measured using a monochromator and a HgCdTe detector (cooled to 77K). The 2D color-coded intensity plots of Figure 30 represent the output spectra as a function of cavity length detuning. Each horizontal "stripe" corresponds to one of the resonant peaks in the OPO output (here only the first 2 peaks were shown, even though we observed more than 10 peaks in total). A horizontal slice from the first oscillation peak is shown in Figure 31. The measured spectrum span was 3–12.5 μm (3333–800 cm^{-1}) at -44 dB level (corresponding to 2.06 octaves), thus reaching the longwave cutoff of GaP.

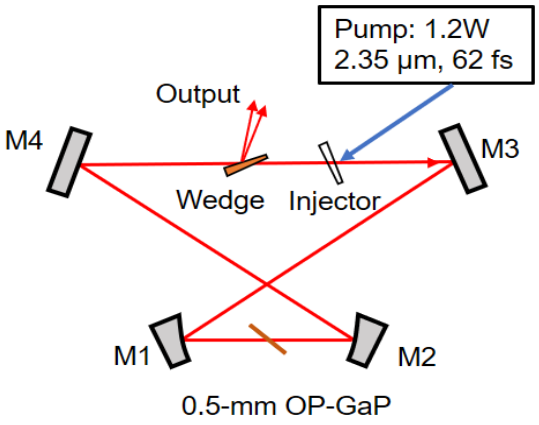

Figure 28: The schematic of the OPO. M1 and M2 are parabolic gold mirrors. M3 and M4 are flat gold mirrors. Injector: the pump injector, which highly reflects the pump and highly transmits the signal and idler waves. Wedge: the 0.3 – 0.9 mm thick ZnSe wedge used for dispersion control and outcoupling.

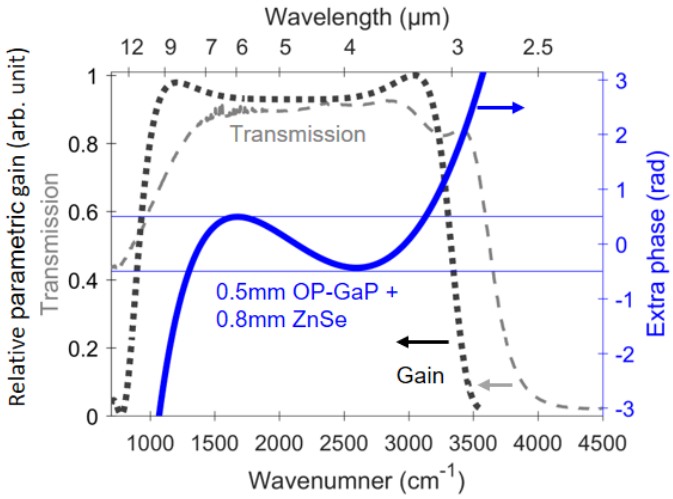

Figure 29: The transmission of the pump injector (dashed grey). The calculated parametric gain of a 0.5-mm OP-GaP crystal for the finite pump spectrum (dotted black). The extra phase for the cavity (solid blue). The blue horizontal line indicates a tolerance of ± 0.5 rad for the extra phase of the cavity.

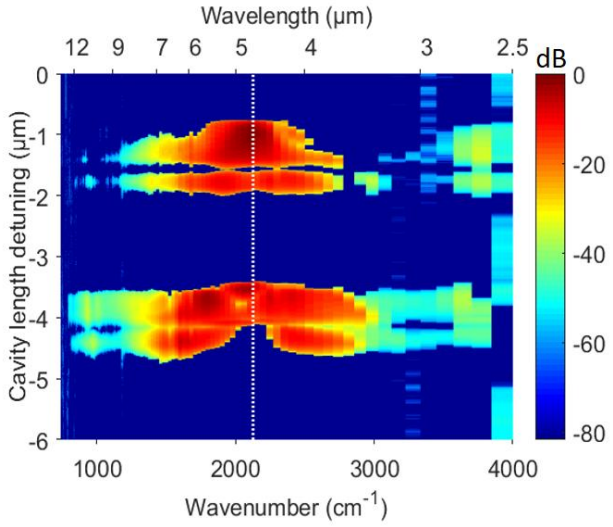

Figure 30: 2D color intensity plots of the output spectra as the resonator length is detuned. The dotted vertical line indicates the generate wavelength 4.7 μm.

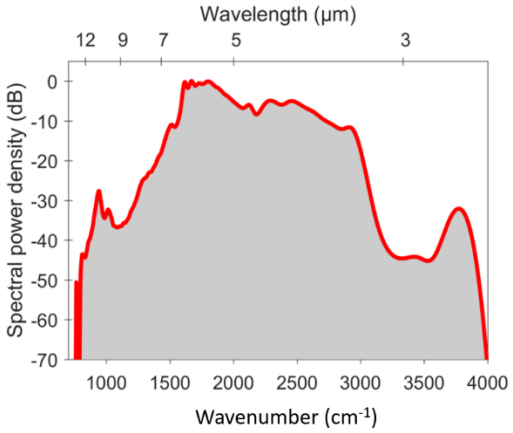

Figure 31: The measured broadest degenerate OPO spectrum.

The oscillation of the spectrum around 1.5 μm is due to the interference between the 1st pulse and the pulse delayed in the cavity. Due the group delay dispersion of the cavity elements, including the OP-GaP crystal, the pump injector and the outcoupling wedge, the pulse generated from the sum frequency has a repetition rate of 79 MHz. The next pulse delayed by the cavity will have a delay relative to the next generated pulse. The delay time can be calculated using the group velocity at 4.7 μm and the wavelength in the near infrared region. The oscillating period in the frequency domain is the inverse of the pulse delay in time domain. The periods of the spectrum and the theory prediction were plotted together in Figure 33. The experiment data matched well with the calculation. The oscillation period decreases as the light frequency increases due to the large difference in the group velocity.

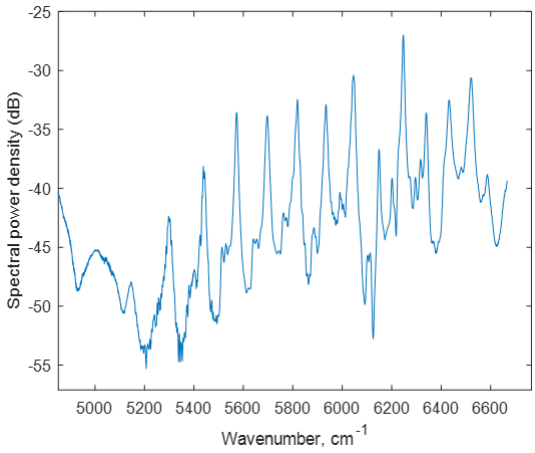

Figure 32: The spectrum of the sum frequency (the signal/idler wave + the pump wave) oscillates with a changing period.

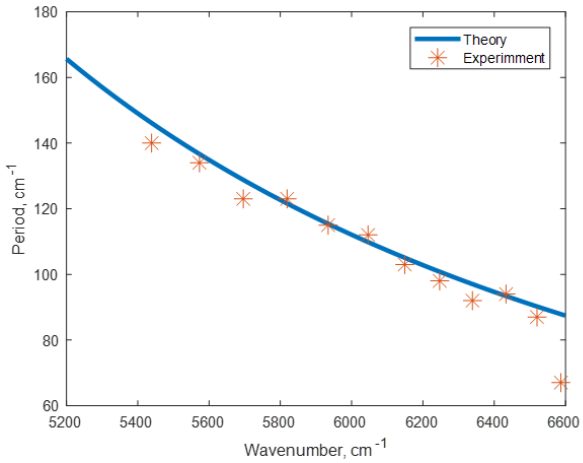

Figure 33: The oscillation periods of the spectrum of the sum frequency wave (red asterisk). The theory prediction calculated using the dispersion of the group velocity (blue curve).

In conclusion, we took full advantage of an ultrafast 2.35-μm laser pumping, combined with the linear and nonlinear properties of the OP-GaP crystal (in particular of its low group velocity dispersion in the OPO range) as well as a new cavity design consisting of all gold-coated mirrors and a low-dispersion pump injector – to achieve an extremely broad spectral output spanning 3–

12.5 μm. When phase-locked, this OPO may become a basis for producing precision ultra-broadband frequency combs in the mid-IR region.

CHAPTER FIVE: OPTICAL PARAMETRIC OSCILLATION IN RANDOM PHASE MATCHING

5.1 Random Phase Matching

An orientation pattern crystal is excellent for making the phase match in isotropic materials. However, it requires a supplicated technique to grow the crystal, and only a few materials are suitable to be orientation pattern in currently. Instead, phase match can be achieved by using polycrystalline materials. As our last step to achieve a broadband spectrum for this project, we demonstrated the random phase matching in the OPO [52]. Random Phase Matching (RPM) not only eliminates the complex grown processes and allow for more materials to be viable in nonlinear processes, but also increases the acceptance bandwidth.

Early in 1966, random phase matching second harmonics generation was observed in a hot-pressed polycrystalline ZnSe and polycrystalline CdTe pumped by a CO_2 laser [53]. Then in 1968, Kurtz et al. reported use random phase matching in power techniques to the nonlinear coefficient of new materials which is difficult to make in bulk [54]. We found the theory he proposed for powder techniques also applied to the phenomena in ceramics. In 2004, Baudrier-Raybaut et al. demonstrated for second harmonics generation that the optimal grain size of polycrystal equals to the coherent length of the material [55]. In 2017, Vasilyev et al. observed strong second harmonics generation in the ZnSe ceramics via random phase matching inside a Cr:ZnSe laser [56]. Thanks to the broad acceptance bandwidth of polycrystalline material, they have been used as a nonlinear gain medium for a number of applications, including nonlinear optical microscopy, autocorrelation measurements, sum- and different-frequency generation, and cascade harmonic generation [57-60]. Most recently, a super-octave spectrum was observed in a Cr^{2+}-doped polycrystalline ZnS

laser system [61]. A multioctave spectrum via simultaneous randomly phase-matched three-wave mixing processes, facilitated by filamentation, has been observed in polycrystalline ZnSe [62]. Several literatures analytically discussed the frequency conversion process based on RPM [55, 60, 63, 64].

To better illustrate the random phase matching, we compared it with other phase matching scenarios in the complex domain (in Figure 34). The arrow indicates the electric field with the length of the arrow representing the amplitude of the electric field, and the angle representing its phase. If the electric field is $E_0 \exp(\omega t + \phi)$. Here E_0 is the amplitude, ϕ is the initial phase. Then the horizontal axis $E_0 \cos(\phi)$, vertical axis is $iE_0 \sin(\phi)$.

In the ideal phase matching case, all the arrows point to the same direction, meaning that the generated electric fields have the same phase. Thus, the electric fields of the light build up quickly. In the no phase matching crystal, the phase of the generated electric phase flips π after the coherent length of the crystal. Thus, the total intensity reverts back to zero after 2 coherent lengths. In quasi phase matching, the orientation of the crystal was flipped every coherent length, thus the electric field will continue to build up with a tradeoff of the efficiency. In the random phase match, since the size and orientation of each grain of the crystal is random, the amplitude and phase of the generated electric field is random as shown by the arrows. Surprisingly, after several grains, the total electric field does not average to zero. Random phase matching in disordered $\chi^{(2)}$ material can be described by the random walk (or drunk sailor's walk) theory. One can imagine a drunkard walking randomly in all directions on the street, but after a while when the drunkard looks back, he finds that he has still managed to walk far away from his original position. In a 2-dimensional

random walk, the travel distance S is merely $L\sqrt{N}$. Here, N is the number of steps and L is the length of each step. It is also used to model the path traced by a molecule as it travels in a liquid or gas), the search path of a foraging animal, the price of a fluctuating stocks and the financial status of a gambler.

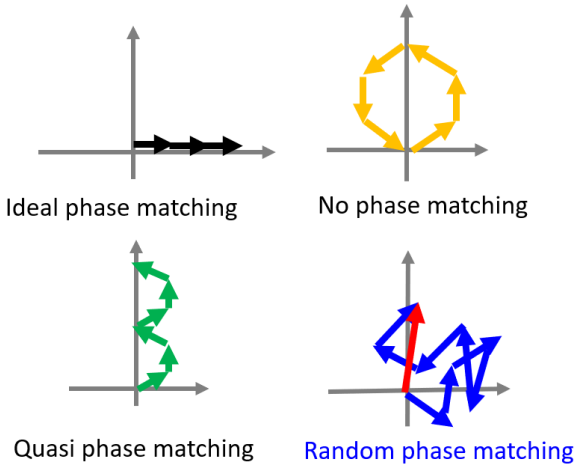

Figure 34: The illustration of different phase matching scenarios.

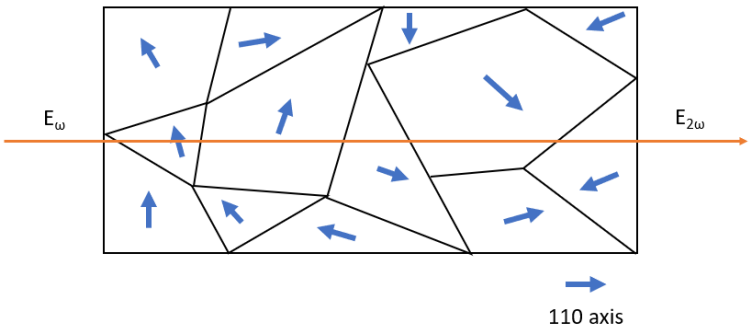

Figure 35: The random orientation of the grains in a polycrystal. The electric field grows $E_{2\omega} \propto N^{1/2}$. N is the number of grains.

Fortunately, RPM does not require orientation patterning, which is a sophisticated process. It will benefit from the 3-wave interactions with an extremely large bandwidth. Nevertheless, the tradeoff

is a slow growth of the signal. The intensity of the signal grows linearly with the length of the sample, as opposed to the quadratic dependence for both perfect phase and quasi-phase matching.

5.2 ZnSe Polycrystal

The high optical quality chemical vapor deposition (CVD) grown polycrystalline is readily available. Our ZnSe samples were prepared as follows: 11mm × 6 mm × 3 mm commercial CVD-grown ceramic ZnSe samples were sealed in quartz ampoules under 10^{-5} Torr vacuum and annealed at 900°C. For nine sets of samples, the annealing time varied from 6 to 10 days with a half-day interval. After annealing, the samples were chemically etched, and the grain size distribution was measured using a microscope. While the average grain size of untreated samples was between 50 and 60 μm, annealing the samples resulted in increasing grain size with time, and reached 100 μm after 8 days of annealing. We used the resulting annealed samples in our experiments, since the grain size was close to the coherence length (107 μm) for our desired three-wave interaction—the optimal condition for RPM [55].

First, we completed the x-y mapping of the ZnSe sample by SHG from 4.7 to 2.35 μm (inverse process with respect of the subharmonic OPO), using a nanosecond $\lambda = 4.7$ μm source. A typical result of SHG mapping is shown in Figure 37. The histogram reveals a broad SHG signal distribution related to variations of the alignment and size of crystalline domains. There are "hot" spots where the efficiency of SHG is 2.5 - 3 times higher than the average (these hot spots were used to achieve oscillation of the OPO). In terms of average (over the histogram) SHG, we observed a linear dependence on sample length, in full accordance with the RPM theory [55].

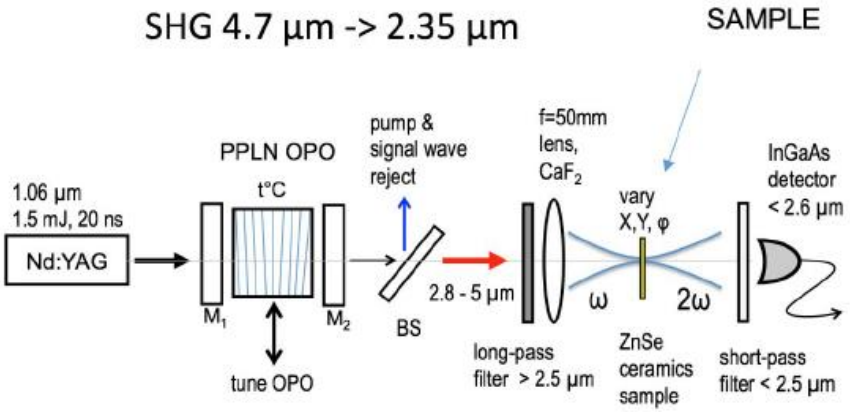

Figure 36: The setup for the ZnSe ceramic characterization via second harmonic generation

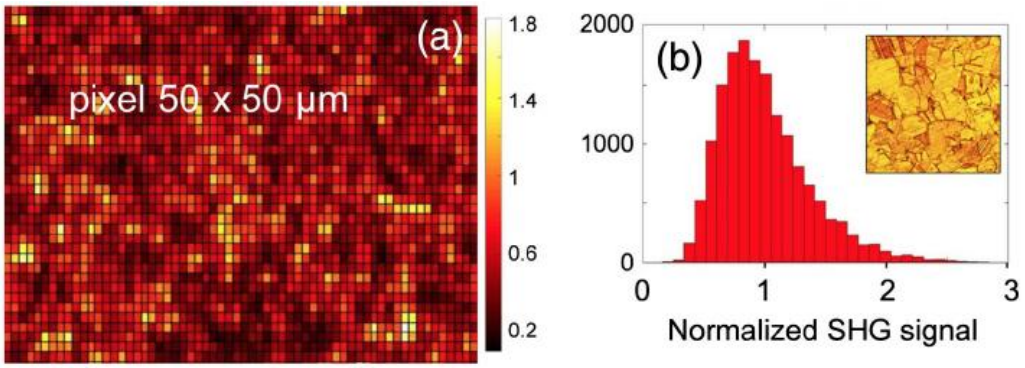

Figure 37: (a) Normalized SHG signal and (b) a histogram for an L = 1.5 mm ZnSe ceramic sample mapped in x–y with 50 µm steps. Inset: 500 µm × 500 µm cross section of a chemically etched ZnSe ceramic sample.

5.3 Polycrystalline ZnSe Based Random Phase Matching OPO

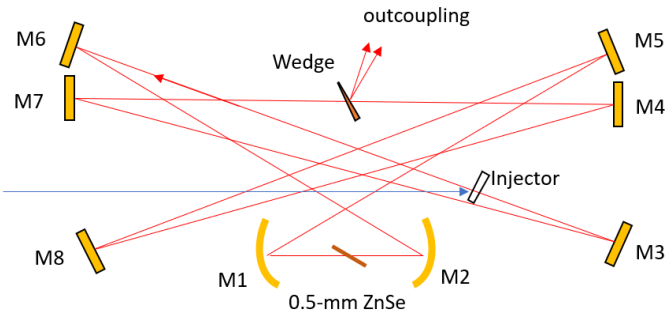

Figure 38: The setup of the OPO. M1 and M2 are parabolic gold mirrors. M3-M8 flat gold mirrors. Injector: the pump injector, which highly reflects the pump and highly transmits the signal and idler waves. Wedge: the 0.3 – 0.9 mm thick ZnSe wedge used for dispersion control and outcoupling. Insert: the output beam profile of the OPO.

The OPO was pumped by a 2.35-μm Cr^{2+}:ZnS laser, with an average power of 1.2 W at a repetition rate of 79 MHz and 62-fs pulse duration. The pump light was coupled to the cavity (Figure 38) via an injector based on a 0.5-mm thick ZnSe wedge that was coated to have >90% reflection for the 2.35-μm pump and >90% transmission for 3.5-7 μm (> 80% for the 2.9 - 8 μm). The pump injector approach has a couple of benefits: 1) it greatly decreases the group delay dispersion typically introduced by a reflective broadband dielectric mirror; 2) the cavity could be built using only gold-coated mirrors, which provide high reflectivity in a broad wavelength range. The ZnSe polycrystal was placed at the Brewster's angle between the two-parabolic gold-coated mirrors (apex radius 30 mm). The cavity was folded with 8 gold-coated mirrors to reduce the footprint. For the pump beam size of ~ 6.6 μm (mode matched to the OPO eigenmode), we estimated the Rayleigh range to be ~ 150 μm inside the ZnSe crystal (corresponding to the focal length ~ 300 μm). Therefore, only a ~0.3 mm ZnSe ceramic is required to fully utilize the pump power. We used a 0.5-mm thick ZnSe ceramic sample in our experiment; it was first characterized in a second harmonics generation

(SHG, 4.7 -> 2.35 μm) experiment via 2D mapping, which assisted us in locating the working points ("hot spots") in the ceramic sample. Once the dispersion of the OPO cavity was optimized by selecting the correct ZnSe thickness of the dispersion control wedge (wedge in Figure 38), it was effortless to run the OPO at different hot spots. With a 3.4% wedge outcoupling, the pump depletion was measured to be 75% at the pump threshold of 450 mW. When we stabilized the OPO cavity length to the degenerate mode, the average power (in two output beams) was around 53 mW (we did not optimize the outcoupling for achieving higher power). The output beam profile was measured by a pyroelectric camera and shown in Figure 39. The measured polarization was linear, but the direction could be either horizontal or slightly deviate from horizontal at different working spots.

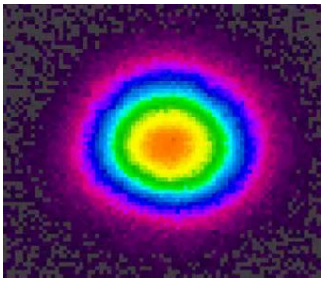

Figure 39: The output beam profile from the OPO

The calculated extra phase per roundtrip of the OPO cavity is shown in Figure 40. (It shows the mismatch between the cavity modes and the OPO modes dictated by the repetition rate of the pump laser.) The ± 0.5 rad is our calculated tolerance for phase deviation. The dashed blue curve in Figure 40 is the transmission of the dielectric pump injector. Also shown is a calculated relative parametric gain, based on our RPM model. One can observe that the main limitation of the spectrum is the extra phase of the OPO.

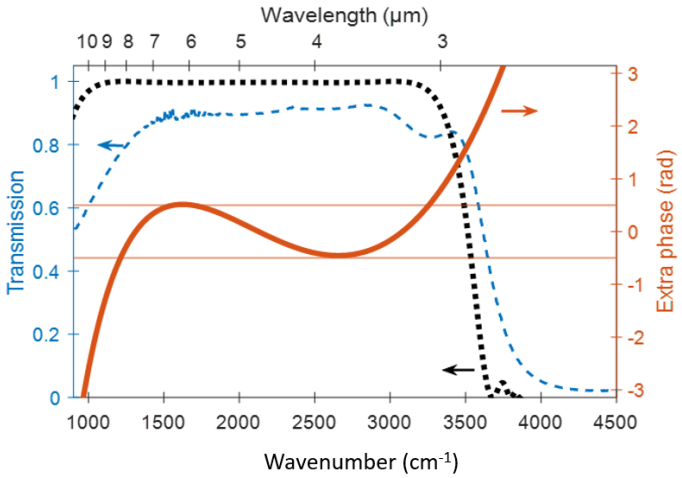

Figure 40: The transmission of the pump injector (dashed blue). The calculated RPM parametric gain for a 0.5-mm ZnSe polycrystal (dotted black). The extra phase for the cavity (solid red). The red horizontal line indicates a tolerance of ± 0.5 rad for the cavity's extra phase.

The OPO spectrum was measured using a monochromator and a HgCdTe (77K) detector. Several long pass filters were used to overcome the limitation of free spectral range. A 2D color intensity plot (an OPO spectrum vs. cavity-length detuning) is shown in Figure 41. The first (from top) oscillation was degenerate and the second was non-degenerate mode with a distinct signal and idler waves. A horizontal slice from the first oscillation is shown in Figure 42. The measured spectral span was 3.17 to 9 μm (3155 – 1100 cm^{-1}) at -55 dB level, which exceeds the bandwidth achieved in our first ceramic OPO, thanks to a shorter ZnSe element and a new cavity design.

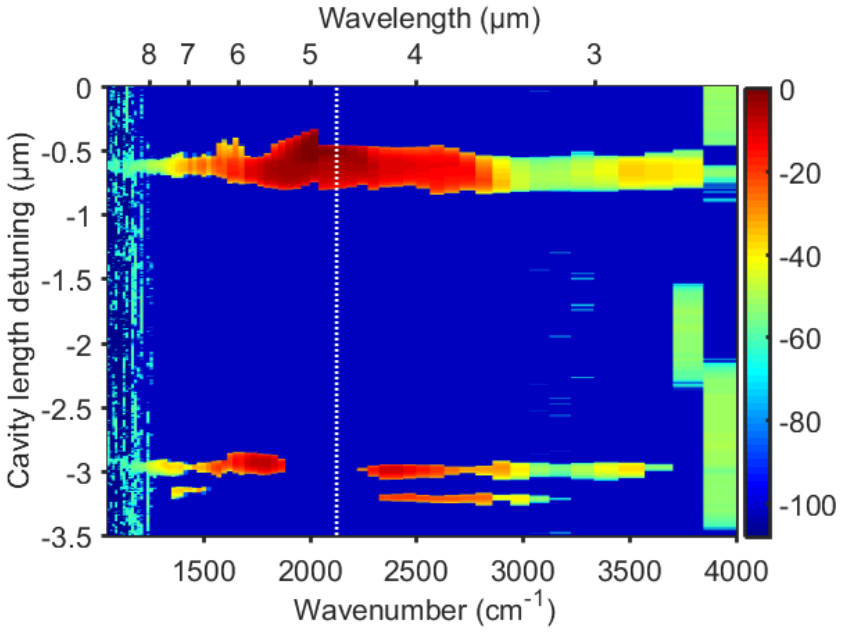

Figure 41: The 2D color intensity plot of spectra as the round trip cavity length. The dotted vertical line indicates the generate wavelength 4.7 μm.

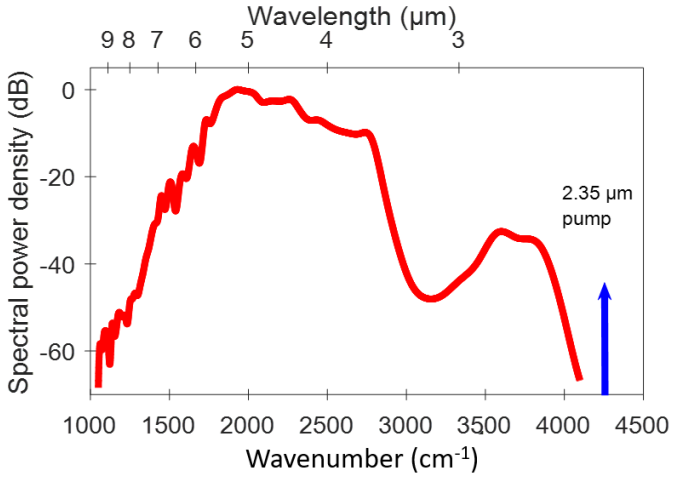

Figure 42: The broadest spectrum generated from the OPO. The blue arrow indicates the position of the pump frequency.

To summarize, we demonstrated an ultrafast subharmonic OPO, where we made use of an extremely thin (0.5-mm) ZnSe ceramic element. A very large gain bandwidth – a characteristic of

RPM, combined with a dispersionless OPO cavity allowed achieving an extremely broad (3.17- 9 μm) output with up to 53 mW average power. This shows great potential for the use of RPM in ultrafast frequency conversion systems, e.g. for producing broadband frequency combs.

CHAPTER SIX: CARRIER ENVELOPE OFFSET FREQUENCY DETECTION

6.1 Introduction

Carrier-envelope offset frequency is the offset between the phase and the maximum of the envelope of the optical pulse. It is due to the mismatch of the group velocity and phase velocity. Carrier envelope offset frequency stabilization is required for a fully stabilized frequency comb. Detecting the carrier envelope offset frequency usually requires the so-called f-to-2f interference. The 2f is achieved via second harmonic generation, the f is generated using the supercontinuum generation. The supercontinuum generation requires high nonlinearity fibers or photonics fibers. Then, an addition optics delay path was required to overlap the f arm and the 2f arm.

The CEO frequencies of the signal and idler waves were related to the pump wave:

$$f_{CEO,s} + f_{CEO,i} = f_{CEO,p} \quad (7)$$

Here $f_{CEO,s}$, $f_{CEO,i}$ and $f_{CEO,p}$ are the CEO frequencies of the signal wave, idler wave, and pump wave, respectively. When the OPO works in the degenerate mode, the $f_{CEO,s}$ and the $f_{CEO,i}$ become identical. Thus, the CEO frequency relation was simplified to

$$2f_{CEO,s,i} = f_{CEO,p} \quad (8)$$

The CEO frequencies of the signal and idler waves are intrinsically locked to the pump wave and equal half of the CEO frequency of the pump wave, meaning that if the subharmonic OPO is pumped with a fully stabilized frequency near infrared frequency comb, it will naturally get a stabilized frequency comb shifted to the mid-infrared region. Vice versa, if the pump source is a

free running frequency comb, by detecting the CEO frequency of the OPO we can use this signal as a feedback to stabilize the CEO of the pump frequency comb. The CEO frequency of the OPO was detailed studied in the papers by Wong et al. [21, 30].

Detecting CEO through f-to-2f beats requires a more than one octave wide spectrum. As a result of low pump threshold and low dispersion cavity, the subharmonic OPOs can easily achieve a multiple octave wide spectrum. Thus, it is possible to detect the carrier offset frequency using the intrinsic beat notes.

6.2 f-to-2f beat in 3-μm OP-GaP OPO

For the OP-GaP OPO pumped by 1.5 μm laser (chapter 4.2), to verify that the octave-wide degenerate spectrum is a single frequency comb, we performed *f-to-2f* beat measurements in the radio frequency (RF) domain. This experiment allows us to characterize coherence properties of a frequency comb and to stabilize its carrier envelope offset frequency (f_{CEO}). Figure 43 represents a conceptual schematic of our *f-to-2f* beat experiment. We used two detectors with a spectral window of 10-100 nm, so that one of them (Det. 1, InAs-based) detects the degenerate wavelength at 3.12 μm, while the other (Det. 2, extended InGaAs-based) detects only 2.35-μm portion of the spectrum (optical frequency 2f), which is 3/4 of the degenerate wavelength, such that the second harmonic (SH) of the 4.7-μm part of the spectrum (optical frequency f), parasitically produced in the OP-GaP inside the OPO cavity, would interfere with the 2.35-μm portion of the spectrum. Both detectors were connected to RF spectrum analyzers (RFSA).

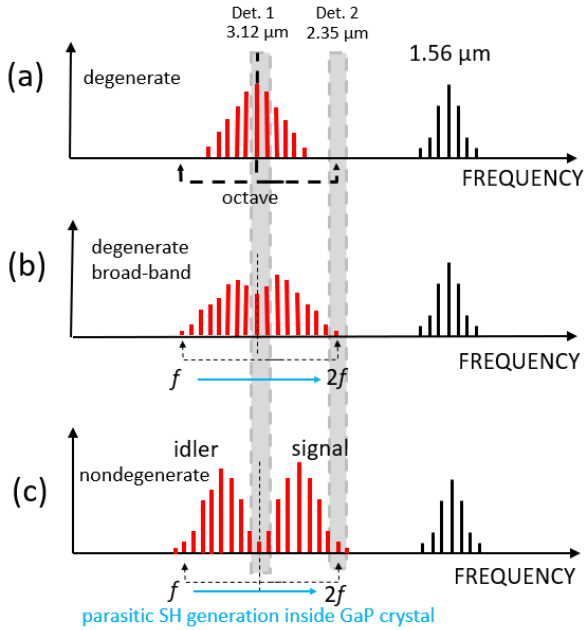

Figure 43: A conceptual picture of the *f*-to-2*f* beat experiment. The spectrum windows for Det. 1 (3.12 µm) and Det. 2 (2.35 µm) are shown as gray dashed boxes. (a) Single comb with less than octave-wide spectrum. (b) Single comb with > one octave-wide spectrum. (c) Nondegenerate scenario with two distinct and overlapping combs. The parasitic SH of the red part of the spectrum in (b,c), parasitically generated inside the GaP crystal, is expected to interfere with the blue part of the spectrum to produce *f*-to-2*f* beats.

When the spectrum is degenerate and less than one octave-wide (Figure 43a), we expect Det. 1 to show only one RF peak, that corresponds to the repetition frequency f_{rep}. Det. 2 is expected to provide no signal, since the spectrum is not broad enough. As the spectrum becomes broader than an octave (Figure 43b), a RFSA signal should appear from Det. 2 in the form of an f_{rep} peak and satellites that correspond to *f-to-2f* beats. At the same time, Det. 1 is expected to show only one peak at f_{rep}. Finally, when the spectrum splits into two distinct but overlapping combs (a nondegenerate mode), Det. 1 would see additional beats between the two combs overlapping at degeneracy. The Det. 2 is expected to still produce an f_{rep} peak and show *f-to-2f* beats which come

from interfering SH of the idler and the OPO signal wave (though now they belong to different combs).

The *f-to-2f* experimental results were close to expectations and are shown in Figure 44. By switching to different cavity resonances, we were able to vary the spectrum of the OPO from degenerate to nondegenerate, similar to [25] and observe RFSA signals originating from Det. 1 and Det. 2. Figure 44 (a)-(c) shows the OPO spectra (linear scale) measured by an FTIR spectrometer, while Figure 44 (d)-(f) shows screenshots of the RFSA for the Det. 1, and Figure 44 (g)-(i) – for Det. 2. The bandwidth of the RFSA was set to 300 kHz.

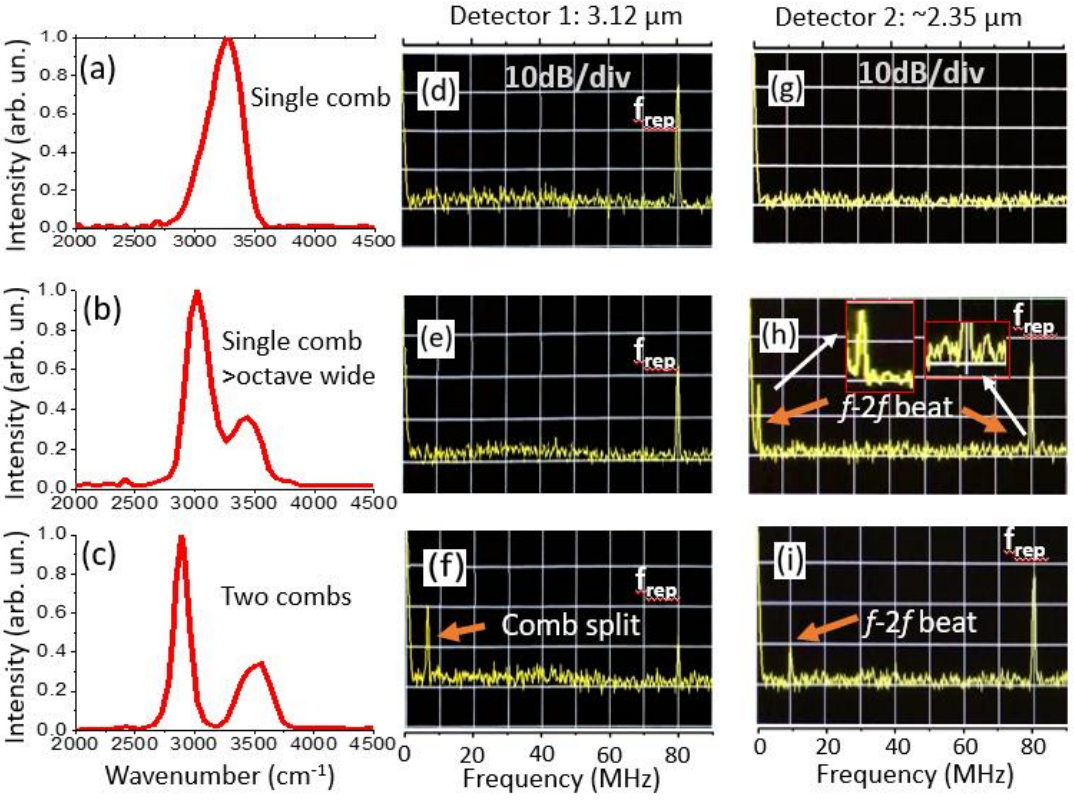

Figure 44: (a)-(c) The linear-scale optical spectra from an FTIR spectrometer. (d)-(f) Corresponding RF spectra from Det. 1 (3.12 μm). (g)-(i) RF spectra from Det. 2 (2.35 μm).

Figure 44a corresponds to a single comb with a less than octave-wide spectrum, while Figure 44b corresponds to a single comb that reached an octave. In the latter case, Det. 1 shows only one peak at f_{rep} (Figure 44 e) that indicates that the OPO output is still one comb. The Det. 2 sees both the *f-to-2f* beats (at 3 MHz) and the f_{rep} peak. For this scenario, the signal to noise ratio for the *f-to-2f* peak was more than 17 dB. Since our detectors had a bandwidth of 50-60 MHz, the observed RF beats near f_{rep} were much weaker than their low-frequency 'mirror-image' counterparts. However, from the second inset on Figure 44h we can still see the two sidebands around f_{rep}, corresponding to *f-to-2f* beats at 3 MHz. In the case of Figure 44c, the OPO is nondegenerate: Det. 1 shows a peak near 6 MHz that suggests a splitting of the OPO combs that overlap at 3.12-μm degeneracy wavelength and produce beats, while Det. 2 shows a peak at 10 MHz due to *f-to-2f* beats originating from SH of the idler interfering with the signal wave.

To further verify that the *f-to-2f* beat comes from a single comb in the scenario of Figure 44b, we recorded RF beats while slowly detuning the cavity length near resonance at a speed of ~ 34 nm/s. Since the CEO frequency of the subharmonic OPO is locked to that of the pump, that is $f_{CEO,OPO} = f_{CEO,pu/2}$, or $f_{CEO,OPO} = f_{CEO,pu/2} + f_{rep/2}$, the beat frequency did not change with cavity detuning, as seen from Figure 45a (a small linear slope is possibly due to the drift of CEO of our free running pump source). In contrast, for the nondegenerate scenario of Figure 44c, we observed a noticeable RF beat frequency change with the cavity length detuning (Figure 45b), since CEO frequencies for the signal and idler waves are no longer locked together.

Given the fact that CEO of a degenerate frequency-divide-by-2 OPO is inherently locked to that of the pump laser, the observed *f-to-2f* frequency beats might be used for self-referencing and

frequency comb stabilization of the pump laser itself, with no need for sacrificing laser power for supercontinuum generation.

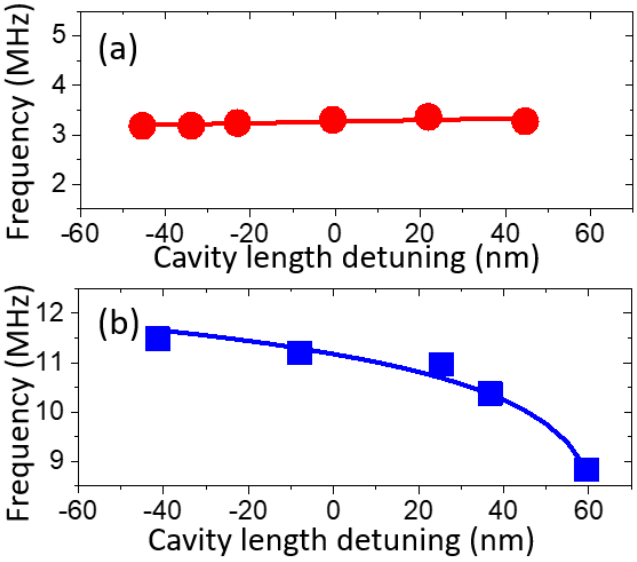

Figure 45: The RF beat frequency versus cavity length detuning from resonance in (a) degenerate scenario and (b) nondegenerate scenario. Solid lines are traces for the eye.

6.3 f-to-2f beat in 4.7-μm OP-GaP OPO

The OP-GaP OPO pumped by the Kerr-lens mode locked Cr:ZnS laser (2.35 μm) yielded a more than two octave spectrum (Chapter 4.3). This broad spectrum promises us the possibility to detect the CEO frequency of the OPO via the f-to-2f beat notes. In the OPO, the photons are generated in pairs; therefore, the best location to observe the f-to-2f beat notes would be 1/3ν and 2/3ν with ν representing the frequency of the pump wave. Thus, for a 2.35 μm laser pumped OPO, 3.5 μm and 7 μm is the ideal location for this observation. A 7 μm wave will have generate parasitic SHG at 3.5 μm because of the high intensity in the cavity.

To detect the f-to-2f beat notes at 3.5 μm, the output beam of the OPO was focused onto a InSb detector. The 3.5 μm band pass filter (FWHM 500 nm) was used remove other wavelengths to increase the signal to noise ratio. A 2.8 μm long pass filter was used to further reduce the power of the pump wave.

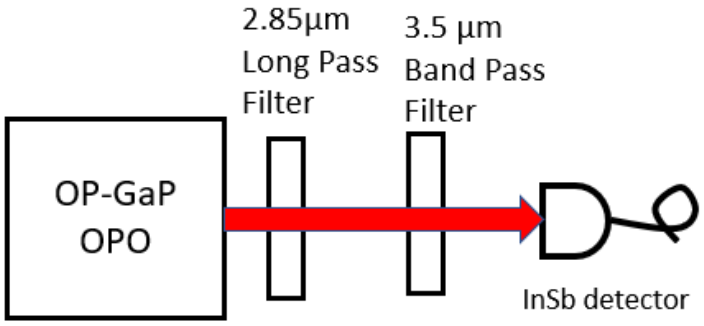

Figure 46: the experiment setup for the f-to-2f beat note detection.

Before measuring the f-to-2f beats, the OPO was stabilized to the first oscillation cavity length. The f-to-2f beat note was recorded by a spectrum analyzer, as shown in Figure 47. The pink and green curves correspond to the CEP frequencies of the OPO when the humidity of the pump laser was changed. When the humidity of the pump Cr:ZnS laser was changed from RH 5% to RH 20% at 20 °C, the CEO frequency drifted from 21 MHz to 25 MHz.

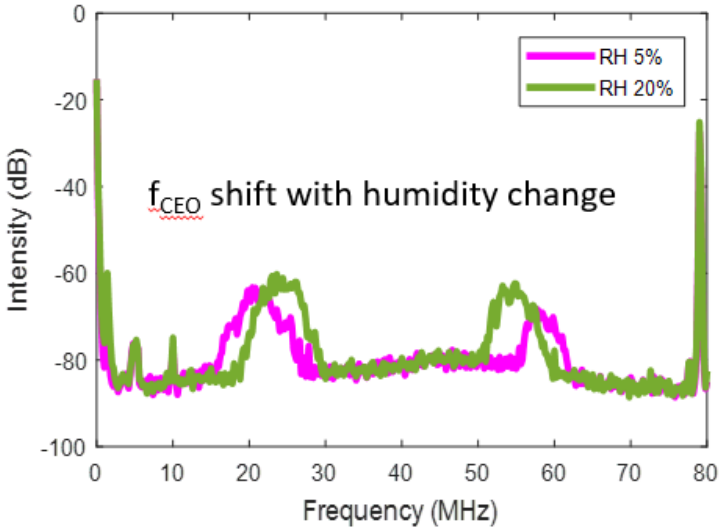

Figure 47. The f-to-2f beat note of the OPO measured at 3.5 µm.

The OPO can work in two different cases, case A and case B. The longitudinal modes of the OPO are different by half of the repetition rate frequency, ½ f_{rep} [29]. The two scenarios can be switched via detuning the cavity length by the wavelength of the pump laser $\lambda_{pump.}$ The frequency of case A is

$$f_A = nf_{rep} + f_{CEO} \quad (9)$$

Here the f_A denotes the frequency of a longitudinal mode in case A, symbol n represents an integer, f_{rep} denotes the repetition rate of the OPO and the pump laser, and f_{CEO} represents the carrier envelope of the OPO.

For case B, the frequency of a longitudinal mode is shifted by half of the repetition rate relative the longitudinal mode in case A.

$$f_B = nf_{rep} + f_{CEO} + \frac{1}{2} f_{rep} \quad (10)$$

Thus, the CEO frequency of case A and case B have a difference of ½ f_{rep}. This property of the subharmonic OPO could be used to verify that the detected RF signal is the CEO frequency of the OPO instead of other signals.

Here we chose the first and second oscillation peaks to measure the CEO frequencies. By optimizing the cavity dispersion, the first and second oscillation peaks could both function at the degenerate mode. The f_{CEO} was measured to be 16.2 MHz in the first peak and 54.6 MHz in the second peak, as shown in Figure 48. The time cost to change between the two cases is less than 1 minute to reduce the slow drift of the CEO of the pump laser. The f_{CEO} and $f_{rep} - f_{CEO}$ is both shown in the RF domain, and they are indistinguishable from one another. The shift of the f_{CEO} is 38.4 MHz, which is approximately ½ f_{rep} (39.5 MHz). The small difference is due to the slow drift of the pump laser's f_{CEO}. The signal to noise ratio of the beat signals were more than 30 dB, which is sufficient to work as a feedback signal to stabilize the CEO frequency of the pump laser.

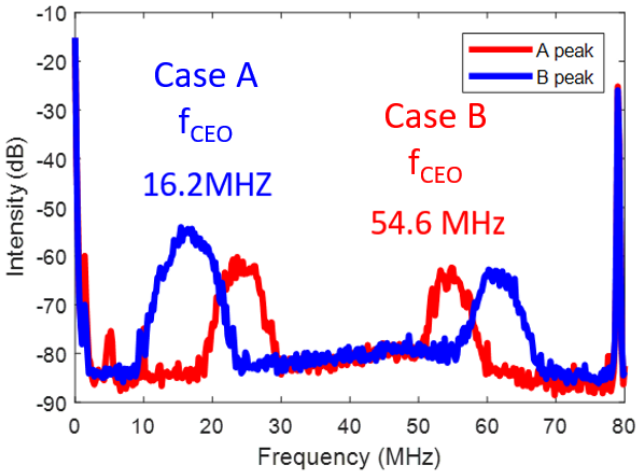

Figure 48. The f_{CEO} of scenario A (blue curve) and scenario B (red curve) corresponding to two OPO oscillation cavity lengths separated by 2.35 μm.

The spectrum of the OPO connected with the pump wave (2.35 μm), the sum frequency of the pump and the mid-infrared wave (centered at 1.56 μm) and the SHG of the pump wave (1.2 μm). If the CEO frequency of the OPO was f_{CEO}, the CEO frequencies for the pump, sum frequency of mid-infrared wave and the pump wave, and SHG of the pump were $2f_{CEO}$, $3f_{CEO}$, and $4f_{CEO}$, respectively. We can detect the CEO frequency though the f_{CEO} - $2f_{CEO}$ beat at the location where the pump wave overlaps with the shorter wavelength part of the OPO, through $3f_{CEO}$ - $2f_{CEO}$ at where the pump wave overlaps with the sum frequency, and $4f_{CEO}$ - $3f_{CEO}$ at where the sum frequency overlaps with the SHG of the pump wave.

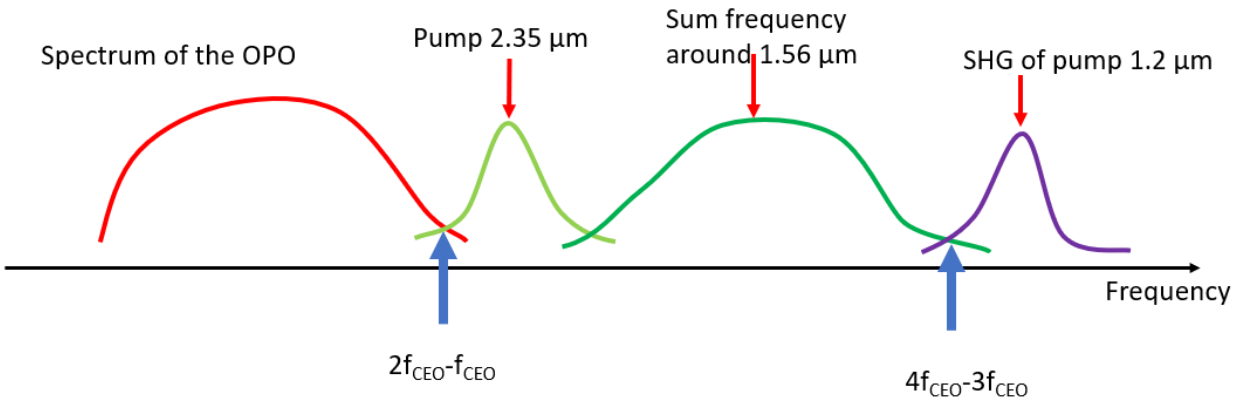

Figure 49. The wavelength locations used to detect the f_{CEO}.

For f_{CEO} - $2f_{CEO}$ between the pump wave and the mid-infrared wave, it is 2.4-2.6 μm. Here, we used an InGaAs detector (G12183-003K, Hamamatsu Photonics). This InGaAs PIN detector has a spectral response range of 0.9 - 2.6 μm and typical bandwidth of 50 MHz. The cutoff wavelength at 2.6 μm is enough to cover the overlap region of the OPO with the mid-infrared laser and has no

response to the longer wave signal. We used a 100 MHz current amplifier with a conversion coefficient of 5E3 V/A. Considering the CEO frequency of the OPO is between 0 to 79 MHz (f_{rep}) and the f_{CEO} and $f_{rep} - f_{CEO}$ will both appear, the bandwidth of the InGaAs detector is enough to observe the signal of the f_{CEO}. The output beam of the OPO passed through a 2.5 µm long pass filter and was then focused on to the detector. The RF signal was amplified by the current amplifier and then displayed by a spectrum analyzer.

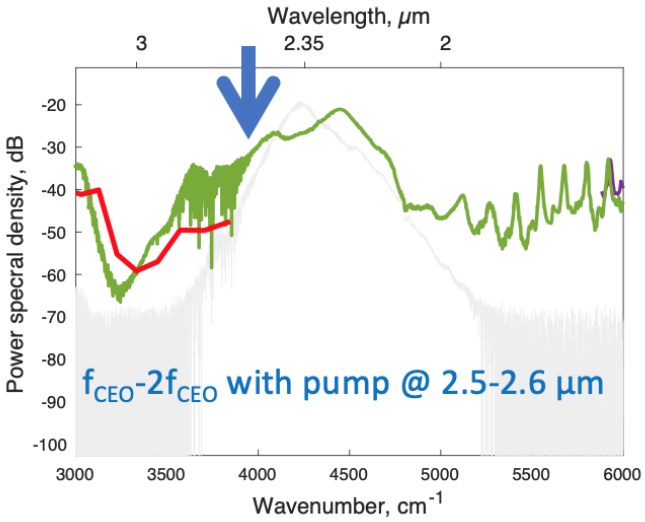

Figure 50. The power spectral density near the from 1.7 – 3.3 µm. The f-to-2f beat note was detected using the power from 2.5 – 2.6 µm.

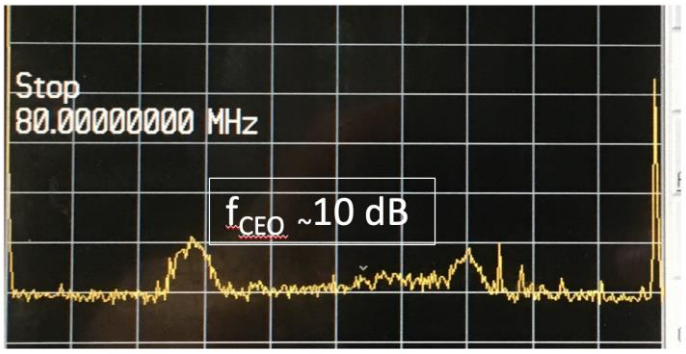

Figure 51. The CEO frequency of the OPO measured at 2.5 – 2.6 µm. Here the f_{CEO} and $f_{rep} - f_{CEO}$ is indistinguishable. The signal to noise ratio is more than 10 dB. The signal at 79 MHz is the repetition rate.

To detect the CEO frequency through the $3f_{CEO} - 4\ f_{CEO}$ frequency, the detector needs to be targeted at the spectrum range where the sum frequency (sum of the signal and idler waves and the pump wave) overlap with the SHG of the pump wave. We focused on the range of 1.2 – 1.5 µm. Here, we used the balanced InGaAs detector (Thorlabs) with a bandwidth of 100 MHz and spectral range 0.8 – 1.7 µm. The beam was collected by a parabolic silver collimator to single mode silica fiber. The spectrum was first measured by an optical spectral analyzer.

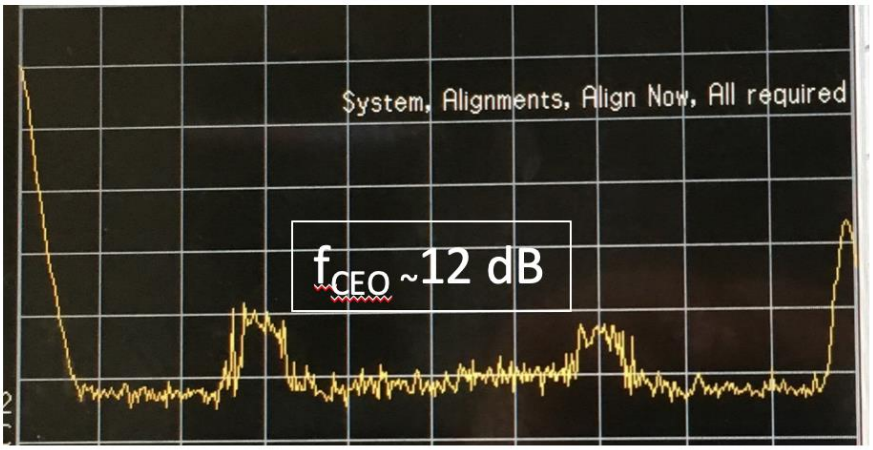

Figure 52. The CEO frequency of the OPO measured at 1.2 – 1.7 μm. Here the f_{CEO} and $f_{rep} - f_{CEO}$ is indistinguishable. The signal to noise ratio is more than 10 dB. The signal at 79 MHz is the repetition rate.

In conclusion, we measured the CEO frequency through the intrinsically f-to-2f beat notes. The f_{CEO} has a more than 30 dB signal to noise ratio and can be further used as feedback to stabilize the CEO frequency of the pump combs.

CHAPTER SEVEN: CONCLUSION AND OUTLOOK

Over the course of this dissertation project, extremely broadband spectra, suitable for generating mid-infrared frequency combs, were demonstrated in subharmonic OPOs using different nonlinear materials. In Chapter three, we achieved 122 mW of average power from the subharmonic OP-GaAs OPO pumped by the ultrafast Cr^{2+}:ZnS laser. The pump slope efficiency was 30%. No roll-off was observed, which indicates that the OPO output power can be further increased by simply increasing the pump power. By optimizing the OPO cavity, the OPO can still function even when the pump power was as low as 8 mW. The observed 85% pump depletion indicates that most of the pump can be converted in to the broadband OPO subharmonic, provided that an appropriate outcoupling is used. The instantaneous spectral span of 2.85 - 8.40 μm (1.56 octaves) achieved from this OPO can serve as the basis for a fully stabilized frequency comb in the mid-IR molecular 'signature' region. Moreover, the spectrum can be further broadened by fabricating an incoupling dielectric mirror with (i) broader reflectivity range and (ii) with compensation of the residual group velocity dispersion.

In Chapter four, we demonstrated the OP-GaP OPO pumped by near- and mid- infrared lasers. For the near-infrared 1.5 μm pumped OP-GaP OPO, we achieved an octave-wide 2.30 – 4.84 μm spectrum in a low-threshold (14-mW) subharmonic OPO, pumped by a free running Er-fiber laser comb. The average comb output power was 29 mW. The spectral span achieved was more than 50% broader, as compared to the prior state-of-the-art based on an Er-fiber-pumped PPLN-based system. For the mid-infrared 2.35 μm pumped OP-GaP OPO, we took the full advantage of the laser pumping, combined with the linear and nonlinear properties of the OP-GaP crystal (in

particular of its low group velocity dispersion in the OPO range) as well as a new cavity design consisting of all gold-coated mirrors and a low-dispersion pump injector – to achieve an extremely broad spectral output spanning 3–12.5 μm. When phase-locked, this OPO may become a basis for producing precision ultra-broadband frequency combs in the mid-IR region.

In Chapter five, we demonstrated an ultrafast subharmonic OPO, where we used ZnSe ceramics samples with different thicknesses (0.5mm, 1mm, 1,5 mm and 2 mm). A very large gain bandwidth –a characteristic of RPM, combined with a dispersionless OPO cavity allowed for achieving an extremely broad (3.17- 9 μm) output with up to 53 mW average power. This shows great potential for the use of RPM in ultrafast frequency conversion systems, e.g. for producing broadband frequency combs.

In Chapter six, the CEO frequency in the subharmonic OPO was studied and directly measured in the output of the OPO since the subharmonic OPO can attain a more than one octave spectrum. Given the fact that CEO of a degenerate frequency-divide-by-2 OPO is inherently locked to that of the pump laser, the observed *f-to-2f* frequency beats might be used for self-referencing and frequency comb stabilization of the pump laser itself, with no need for sacrificing laser power for supercontinuum generation.

These broadband OPOs are ideal for generating mid-infrared frequency combs and are exemplary instruments to detect multi molecular species with a parts-per-billion sensitivity. Furthermore, these broad bandwidth spectra are coherently locked to the pump combs and can be utilized for multiple applications including precision spectroscopy, dual combs spectroscopy, remote sensing, breath analysis and combustion diagnostic.

LIST OF PUBLICATIONS

1. T. Kawamori, Q. Ru, and K. L. Vodopyanov, "Comprehensive Model for Randomly Phase-Matched Frequency Conversion in Zinc-Blende Polycrystals and Experimental Results for ZnSe," Physical Review Applied 11, 054015 (2019).
2. T. Tomberg, A. Muraviev, **Q. Ru**, and K. L. Vodopyanov, "Background-free broadband absorption spectroscopy based on interferometric suppression with a sign-inverted waveform," Optica **6**, 147-151 (2019).
3. V. Smolski, S. Vasilyev, I. Moskalev, M. Mirov, **Q. Ru**, A. Muraviev, P. Schunemann, S. Mirov, V. Gapontsev, and K. Vodopyanov, "Half-Watt average power femtosecond source spanning 3–8 μm based on subharmonic generation in GaAs," Appl. Phys. B **124**, 101 (2018).
4. **Q. Ru**, Z. E. Loparo, X. Zhang, S. Crystal, S. Vasu, P. G. Schunemann, and K. L. Vodopyanov, "Self-referenced octave-wide subharmonic GaP optical parametric oscillator centered at 3 μm and pumped by an Er-fiber laser," Opt. Lett. **42**, 4756-4759 (2017).
5. **Q. Ru**, N. Lee, X. Chen, K. Zhong, G. Tsoy, M. Mirov, S. Vasilyev, S. B. Mirov, and K. L. Vodopyanov, "Optical parametric oscillation in a random polycrystalline medium," Optica **4**, 617-618 (2017).
6. F. Gou, F. Peng, **Q. Ru**, Y.-H. Lee, H. Chen, Z. He, T. Zhan, K. L. Vodopyanov, and S.-T. Wu, "Mid-wave infrared beam steering based on high-efficiency liquid crystal diffractive waveplates," Opt. Express **25**, 22404-22410 (2017).

REFERENCES

[1] T. W. Hänsch, "Nobel Lecture: Passion for precision," Reviews of Modern Physics **78**, 1297-1309 (2006).

[2] J. L. Hall, "Nobel Lecture: Defining and measuring optical frequencies," Reviews of Modern Physics **78**, 1279-1295 (2006).

[3] S. A. Diddams, "The evolving optical frequency comb [Invited]," J. Opt. Soc. Am. B **27**, B51-B62 (2010).

[4] T. Ideguchi, B. Bernhardt, G. Guelachvili, T. W. Hänsch, and N. Picqué, "Raman-induced Kerr-effect dual-comb spectroscopy," Opt. Lett. **37**, 4498-4500 (2012).

[5] B. Lomsadze and S. T. Cundiff, "Frequency combs enable rapid and high-resolution multidimensional coherent spectroscopy," Science **357**, 1389-1391 (2017).

[6] N. Picqué and T. W. Hänsch, "Frequency comb spectroscopy," Nature Photonics **13**, 146-157 (2019).

[7] M. L. Weichman, P. B. Changala, J. Ye, Z. Chen, M. Yan, and N. Picqué, "Broadband molecular spectroscopy with optical frequency combs," J. Mol. Spectrosc. **355**, 66-78 (2019).

[8] A. Foltynowicz, P. Masłowski, T. Ban, F. Adler, K. Cossel, T. Briles, and J. Ye, "Optical frequency comb spectroscopy," Faraday Discuss. **150**, 23-31 (2011).

[9] S. T. Cundiff and J. Ye, "Colloquium: Femtosecond optical frequency combs," Reviews of Modern Physics **75**, 325-342 (2003).

[10] R. K. Altmann, L. S. Dreissen, E. J. Salumbides, W. Ubachs, and K. S. E. Eikema, "Deep-Ultraviolet Frequency Metrology of H_2 for Tests of Molecular Quantum Theory," Phys. Rev. Lett. **120**, 043204 (2018).

[11] A. V. Muraviev, V. O. Smolski, Z. E. Loparo, and K. L. Vodopyanov, "Massively parallel sensing of trace molecules and their isotopologues with broadband subharmonic mid-infrared frequency combs," Nature Photonics **12**, 209-214 (2018).

[12] G. Ycas, F. R. Giorgetta, E. Baumann, I. Coddington, D. Herman, S. A. Diddams, and N. R. Newbury, "High-coherence mid-infrared dual-comb spectroscopy spanning 2.6 to 5.2 μm," Nature Photonics **12**, 202-208 (2018).

[13] N. Picqué and T. W. Hänsch, "Mid-IR Spectroscopic Sensing," Optics and Photonics News **30**, 26-33 (2019).

[14] A. Schliesser, N. Picqué, and T. W. Hänsch, "Mid-infrared frequency combs," Nature Photonics **6**, 440 (2012).

[15] K. F. Lee, J. Jiang, C. Mohr, J. Bethge, M. E. Fermann, N. Leindecker, K. L. Vodopyanov, P. G. Schunemann, and I. Hartl, "Carrier envelope offset frequency of a doubly resonant, nondegenerate, mid-infrared GaAs optical parametric oscillator," Opt. Lett. **38**, 1191-1193 (2013).

[16] F. Adler, K. C. Cossel, M. J. Thorpe, I. Hartl, M. E. Fermann, and J. Ye, "Phase-stabilized, 1.5 W frequency comb at 2.8–4.8 μm," Opt. Lett. **34**, 1330-1332 (2009).

[17] B. J. Bjork, T. Q. Bui, O. H. Heckl, P. B. Changala, B. Spaun, P. Heu, D. Follman, C. Deutsch, G. D. Cole, M. Aspelmeyer, M. Okumura, and J. Ye, "Direct frequency comb measurement of OD + CO → DOCO kinetics," Science **354**, 444-448 (2016).

[18] B. Spaun, P. B. Changala, D. Patterson, B. J. Bjork, O. H. Heckl, J. M. Doyle, and J. Ye, "Continuous probing of cold complex molecules with infrared frequency comb spectroscopy," Nature **533**, 517 (2016).

[19] M. Faraday, "On a Peculiar Class of Acoustical Figures; and on Certain Forms Assumed by Groups of Particles upon Vibrating Elastic Surfaces," Philosophical Transactions of the Royal Society of London **121**, 299-340 (1831).

[20] R. Hamerly, A. Marandi, M. Jankowski, M. M. Fejer, Y. Yamamoto, and H. Mabuchi, "Reduced models and design principles for half-harmonic generation in synchronously pumped optical parametric oscillators," Physical Review A **94**, 063809 (2016).

[21] S. T. Wong, K. L. Vodopyanov, and R. L. Byer, "Self-phase-locked divide-by-2 optical parametric oscillator as a broadband frequency comb source," J. Opt. Soc. Am. B **27**, 876-882 (2010).

[22] J. A. Armstrong, N. Bloembergen, J. Ducuing, and P. S. Pershan, "Interactions between Light Waves in a Nonlinear Dielectric," Physical Review **127**, 1918-1939 (1962).

[23] N. Leindecker, A. Marandi, R. L. Byer, and K. L. Vodopyanov, "Broadband degenerate OPO for mid-infrared frequency comb generation," Opt. Express **19**, 6296-6302 (2011).

[24] N. Leindecker, A. Marandi, R. L. Byer, K. L. Vodopyanov, J. Jiang, I. Hartl, M. Fermann, and P. G. Schunemann, "Octave-spanning ultrafast OPO with 2.6-6.1μm instantaneous bandwidth pumped by femtosecond Tm-fiber laser," Opt. Express **20**, 7046-7053 (2012).

[25] V. O. Smolski, H. Yang, S. D. Gorelov, P. G. Schunemann, and K. L. Vodopyanov, "Coherence properties of a 2.6–7.5 μm frequency comb produced as a subharmonic of a Tm-fiber laser," Opt. Lett. **41**, 1388-1391 (2016).

[26] K. L. Vodopyanov, E. Sorokin, I. T. Sorokina, and P. G. Schunemann, "Mid-IR frequency comb source spanning 4.4–5.4 μm based on subharmonic GaAs optical parametric oscillator," Opt. Lett. **36**, 2275-2277 (2011).

[27] V. O. Smolski, S. Vasilyev, P. G. Schunemann, S. B. Mirov, and K. L. Vodopyanov, "Cr:ZnS laser-pumped subharmonic GaAs optical parametric oscillator with the spectrum spanning 3.6-5.6 μm," Opt. Lett. **40**, 2906-2908 (2015).

[28] J. H. Sun, B. J. S. Gale, and D. T. Reid, "Composite frequency comb spanning 0.4-2.4 μm from a phase-controlled femtosecond Ti:sapphire laser and synchronously pumped optical parametric oscillator," Opt. Lett. **32**, 1414-1416 (2007).

[29] A. Marandi, N. C. Leindecker, V. Pervak, R. L. Byer, and K. L. Vodopyanov, "Coherence properties of a broadband femtosecond mid-IR optical parametric oscillator operating at degeneracy," Opt. Express **20**, 7255-7262 (2012).

[30] S. T. Wong, T. Plettner, K. L. Vodopyanov, K. Urbanek, M. Digonnet, and R. L. Byer, "Self-phase-locked degenerate femtosecond optical parametric oscillator," Opt. Lett. **33**, 1896-1898 (2008).

[31] K. F. Lee, N. Granzow, M. A. Schmidt, W. Chang, L. Wang, Q. Coulombier, J. Troles, N. Leindecker, K. L. Vodopyanov, P. G. Schunemann, M. E. Fermann, P. S. J. Russell, and I. Hartl, "Midinfrared frequency combs from coherent supercontinuum in chalcogenide and optical parametric oscillation," Opt. Lett. **39**, 2056-2059 (2014).

[32] K. F. Lee, C. Mohr, J. Jiang, P. G. Schunemann, K. L. Vodopyanov, and M. E. Fermann, "Midinfrared frequency comb from self-stable degenerate GaAs optical parametric oscillator," Opt. Express **23**, 26596-26603 (2015).

[33] X. P. Hu, P. Xu, and S. N. Zhu, "Engineered quasi-phase-matching for laser techniques [Invited]," Photon. Res. **1**, 171-185 (2013).

[34] L. E. Myers, R. C. Eckardt, M. M. Fejer, R. L. Byer, W. R. Bosenberg, and J. W. Pierce, "Quasi-phase-matched optical parametric oscillators in bulk periodically poled LiNbO3," J. Opt. Soc. Am. B **12**, 2102-2116 (1995).

[35] A. Galvanauskas, M. A. Arbore, M. M. Fejer, M. E. Fermann, and D. Harter, "Fiber-laser-based femtosecond parametric generator in bulk periodically poled LiNbO3," Opt. Lett. **22**, 105-107 (1997).

[36] S. B. Mirov, V. V. Fedorov, D. Martyshkin, I. S. Moskalev, M. Mirov, and S. Vasilyev, "Progress in mid-IR lasers based on Cr and Fe-doped II–VI chalcogenides," IEEE Journal of selected topics in quantum electronics **21**, 292-310 (2015).

[37] S. Vasilyev, M. Mirov, and V. Gapontsev, "Mid-IR Kerr-Lens Mode-Locked Polycrystalline Cr^{2+}:ZnS Laser with 0.5 MW Peak Power," in *Advanced Solid State Lasers*, OSA Technical Digest (online) (Optical Society of America, 2015), AW4A.3.

[38] S. Vasilyev, I. Moskalev, M. Mirov, S. Mirov, and V. Gapontsev, "Multi-Watt mid-IR femtosecond polycrystalline Cr^{2+}:ZnS and Cr^{2+}:ZnSe laser amplifiers with the spectrum spanning 2.0-2.6 μm," Opt. Express **24**, 1616-1623 (2016).

[39] S. Vasilyev, I. Moskalev, M. Mirov, V. Smolski, S. Mirov, and V. Gapontsev, "Kerr-Lens Mode-Locked Middle IR Polycrystalline Cr:ZnS Laser with a Repetition Rate 1.2 GHz," in *Lasers Congress 2016 (ASSL, LSC, LAC)*, OSA Technical Digest (online) (Optical Society of America, 2016), AW1A.2.

[40] T. Skauli, K. L. Vodopyanov, T. J. Pinguet, A. Schober, O. Levi, L. A. Eyres, M. M. Fejer, J. S. Harris, B. Gerard, L. Becouarn, E. Lallier, and G. Arisholm, "Measurement of the nonlinear

coefficient of orientation-patterned GaAs and demonstration of highly efficient second-harmonic generation," Opt. Lett. **27**, 628-630 (2002).

[41] P. G. Schunemann, "Recent advances in all-epitaxial growth and processing of OP-GaAs," in *Laser Congress 2018 (ASSL)*, OSA Technical Digest (Optical Society of America, 2018), ATu4A.6.

[42] Q. Ru, K. Zhong, N. P. Lee, Z. E. Loparo, P. G. Schunemann, S. Vasilyev, S. B. Mirov, and K. L. Vodopyanov, *Instantaneous spectral span of 2.85 - 8.40 μm achieved in a Cr:ZnS laser pumped subharmonic OPO*, SPIE LASE (SPIE, 2017), Vol. 10088, p. 7.

[43] L.-J. Chen, A. J. Benedick, J. R. Birge, M. Y. Sander, and F. X. Kärtner, "Octave-spanning, dual-output 2.166 GHz Ti:sapphire laser," Opt. Express **16**, 20699-20705 (2008).

[44] P. G. Schunemann, L. A. Pomeranz, and D. J. Magarrell, "First OPO based on orientation-patterned gallium phosphide (OP-GaP)," in *CLEO: 2015*, OSA Technical Digest (online) (Optical Society of America, 2015), SW3O.1.

[45] L. Maidment, P. G. Schunemann, and D. T. Reid, "Molecular fingerprint-region spectroscopy from 5 to 12 μm using an orientation-patterned gallium phosphide optical parametric oscillator," Opt. Lett. **41**, 4261-4264 (2016).

[46] E. Sorokin, A. Marandi, P. G. Schunemann, M. M. Fejer, R. L. Byer, and I. T. Sorokina, "Efficient half-harmonic generation of three-optical-cycle mid-IR frequency comb around 4 μm using OP-GaP," Opt. Express **26**, 9963-9971 (2018).

[47] W. C. Hurlbut, Y.-S. Lee, K. L. Vodopyanov, P. S. Kuo, and M. M. Fejer, "Multiphoton absorption and nonlinear refraction of GaAs in the mid-infrared," Opt. Lett. **32**, 668-670 (2007).

[48] O. H. Heckl, B. J. Bjork, G. Winkler, P. Bryan Changala, B. Spaun, G. Porat, T. Q. Bui, K. F. Lee, J. Jiang, M. E. Fermann, P. G. Schunemann, and J. Ye, "Three-photon absorption in optical parametric oscillators based on OP-GaAs," Opt. Lett. **41**, 5405-5408 (2016).

[49] P. G. Schunemann, D. J. Magarrell, and L. A. Pomeranz, "HVPE of Orientation-Patterned Gallium Phosphide (OP-GaP) with Novel Quasi-Phasematched Device Structures," in *Conference on Lasers and Electro-Optics*, OSA Technical Digest (online) (Optical Society of America, 2018), STh4F.1.

[50] K. L. Vodopyanov, S. T. Wong, and R. L. Byer, "Infrared frequency comb methods, arrangements and applications," US Patent 8,384,990 (2013).

[51] Q. Ru, Z. E. Loparo, X. Zhang, S. Crystal, S. Vasu, P. G. Schunemann, and K. L. Vodopyanov, "Self-referenced octave-wide subharmonic GaP optical parametric oscillator centered at 3 μm and pumped by an Er-fiber laser," Opt. Lett. **42**, 4756-4759 (2017).

[52] Q. Ru, N. Lee, X. Chen, K. Zhong, G. Tsoy, M. Mirov, S. Vasilyev, S. B. Mirov, and K. L. Vodopyanov, "Optical parametric oscillation in a random polycrystalline medium," Optica **4**, 617-618 (2017).

[53] C. K. N. Patel, "Optical Harmonic Generation in the Infrared Using a CO_2 Laser," Phys. Rev. Lett. **16**, 613-616 (1966).

[54] S. K. Kurtz and T. T. Perry, "A Powder Technique for the Evaluation of Nonlinear Optical Materials," J. Appl. Phys. **39**, 3798-3813 (1968).

[55] M. Baudrier-Raybaut, R. Haïdar, P. Kupecek, P. Lemasson, and E. Rosencher, "Random quasi-phase-matching in bulk polycrystalline isotropic nonlinear materials," Nature **432**, 374 (2004).

[56] S. Vasilyev, I. Moskalev, M. Mirov, V. Smolski, S. Mirov, and V. Gapontsev, "Ultrafast middle-IR lasers and amplifiers based on polycrystalline Cr:ZnS and Cr:ZnSe," Opt. Mater. Express **7**, 2636-2650 (2017).

[57] R. Hellwarth and P. Christensen, "Nonlinear optical microscopic examination of structure in polycrystalline ZnSe," Optics Communications **12**, 318-322 (1974).

[58] R. Kesselring, A. W. Kälin, and F. K. Kneubühl, "Mid-infrared nonlinear phenomena in polycrystalline semiconductors," Appl. Phys. B **55**, 437-445 (1992).

[59] T. D. Chinh, W. Seibt, and K. Siegbahn, "Dot patterns from second-harmonic and sum-frequency generation in polycrystalline ZnSe," J. Appl. Phys. **90**, 2612-2614 (2001).

[60] R. Kupfer, H. J. Quevedo, H. L. Smith, L. A. Lisi, G. Tiwari, C. G. Richmond, B. B. Bowers, L. Fang, and B. M. Hegelich, "Cascade random-quasi-phase-matched harmonic generation in polycrystalline ZnSe," J. Appl. Phys. **124**, 243102 (2018).

[61] S. Vasilyev, I. Moskalev, V. Smolski, J. Peppers, M. Mirov, V. Fedorov, D. Martyshkin, S. Mirov, and V. Gapontsev, "Octave-spanning Cr:ZnS femtosecond laser with intrinsic nonlinear interferometry," Optica **6**, 126-127 (2019).

[62] R. Šuminas, G. Tamošauskas, G. Valiulis, V. Jukna, A. Couairon, and A. Dubietis, "Multi-octave spanning nonlinear interactions induced by femtosecond filamentation in polycrystalline ZnSe," Appl. Phys. Lett. **110**, 241106 (2017).

[63] E. Y. Morozov and A. S. Chirkin, "Stochastic quasi-phase matching in nonlinear-optical crystals with an irregular domain structure," Quantum Electronics **34**, 227-232 (2004).

[64] X. Vidal and J. Martorell, "Generation of Light in Media with a Random Distribution of Nonlinear Domains," Phys. Rev. Lett. **97**, 013902 (2006).